A Comprehensive Comparison of Relativistic Particle Integrators

B. Ripperda[1] , F. Bacchini[1] , J. Teunissen[1] , C. Xia[1] , O. Porth[2] , L. Sironi[3] , G. Lapenta[1] , and R. Keppens[1]

[1] Centre for Mathematical Plasma Astrophysics, Department of Mathematics, KU Leuven, Celestijnenlaan 200B, B-3001 Leuven, Belgium
[2] Institut fur Theoretische Physik, Max-von-Laue-Str. 1, D-60438 Frankfurt, Germany
[3] Department of Astronomy, Columbia University, 550 W 120th St, New York, NY 10027, USA

Abstract

We compare relativistic particle integrators commonly used in plasma physics, showing several test cases relevant for astrophysics. Three explicit particle pushers are considered, namely, the Boris, Vay, and Higuera–Cary schemes. We also present a new relativistic fully implicit particle integrator that is energy conserving. Furthermore, a method based on the relativistic guiding center approximation is included. The algorithms are described such that they can be readily implemented in magnetohydrodynamics codes or Particle-in-Cell codes. Our comparison focuses on the strengths and key features of the particle integrators. We test the conservation of invariants of motion and the accuracy of particle drift dynamics in highly relativistic, mildly relativistic, and non-relativistic settings. The methods are compared in idealized test cases, i.e., without considering feedback onto the electrodynamic fields, collisions, pair creation, or radiation. The test cases include uniform electric and magnetic fields, $E \times B$ fields, force-free fields, and setups relevant for high-energy astrophysics, e.g., a magnetic mirror, a magnetic dipole, and a magnetic null. These tests have direct relevance for particle acceleration in shocks and in magnetic reconnection.

Key words: acceleration of particles – methods: numerical – plasmas – relativistic processes

1. Introduction

In astrophysics, relativistic magnetized flows are ubiquitous around compact objects like black holes and neutron stars. Typical plasma processes in these regimes cover a large range of energy scales, timescales, and length scales, from global fluid scales to microscopic particle scales. Although the large scales can often be captured within the magnetohydrodynamics (MHD) approximation, the small scales cannot. The macroscopic evolution of a plasma often develops relatively slowly, even in relativistic regimes. The macroscopic scale is, however, tightly coupled to faster phenomena occurring at smaller scales. Many of these phenomena occur in relativistic magnetized plasmas. In the magnetosphere of a compact object, the typical magnetic field can become extremely strong. But in general, even for weaker magnetic fields, the plasma consists of relativistic particles. In these conditions, relativistic effects have to be taken into account for both the global flow and the particles. However, even in the solar corona or the Earth's magnetosphere, where global flows are non-relativistic, particles can accelerate to mildly relativistic energies (Li et al. 2015; Ripperda et al. 2017a, 2017b).

At relativistic energies, the particle equations of motion become nonlinear due to the presence of the Lorentz factor in the momentum of the particle. There are several numerical methods to treat relativistic particle motion accurately. Here, we aim to test a selection of available classical and recent explicit leapfrog methods (Boris 1970; Vay 2008; Higuera & Cary 2017). We also present and test a newly implemented fully implicit relativistic method that conserves energy exactly. We apply these methods to known tests for which analytic solutions are available and to more involved setups that are relevant for high-energy astrophysics. Therefore, in the first part of this paper, we focus on highly relativistic particles with Lorentz factors much larger than unity, such that the differences between the schemes are well pronounced. We ignore quantum electrodynamics effects, radiation, and collisions, and we focus on relativistic particle motion rather than on the feedback of the particles on the electromagnetic fields. It is, however, straightforward to incorporate these effects in MHD or Particle-in-Cell (PIC) codes.

We also compare the obtained particle trajectories to the relativistic guiding center equations of motion. These equations are solved via an explicit fourth-order Runge–Kutta method (Ripperda et al. 2017a) and compared to the full solution in order to determine in which regimes gyration can be neglected. The guiding center method has the advantage that the gyration of particles can be ignored, under appropriate assumptions, so that the numerical solution is cheaper to obtain. It also gives additional information on drift motions and acceleration mechanisms for the particles. In the second part of this paper, the comparison of the various integrators is done in the Newtonian limit, with Lorentz factors close to unity. In this limit, all explicit schemes converge to the same solution, and the implicit scheme does, too, for a sufficiently small time step. The obtained differences in the results can then be unequivocally assigned to the guiding center approximation (GCA).

The accuracy and performance of all methods are tested for various regimes, from Newtonian to highly relativistic energies, in idealized setups relevant for astrophysics. Accuracy is assessed by determining how (approximately) how well the conserved quantities are evolved. This study focuses on the particle pusher, and we only consider static, spatially uniform, and nonuniform electromagnetic fields. The relativistic pushers considered are commonly used in MHD codes to evolve particles in a global (magnetized) fluid flow (Bai et al. 2015; Porth et al. 2016; Ripperda et al. 2017a, 2017b) and in PIC codes to evolve both particles and electromagnetic fields (Buneman 1993; Spitkovsky 2005; Bowers et al. 2008; Lapenta & Markidis 2011). In both methods, the electromagnetic fields typically have to be interpolated to the particle position. Interpolation errors are tested here by feeding the pusher with an interpolated, spatially varying field that is known exactly at the particle location, and then we

compare the results with those for an analytic, spatially varying field.

The particle integrators considered are presented in Section 2. The methods are presented here as independent algorithms and can therefore be readily implemented in any PIC or fluid code to evolve particles interacting with electromagnetic fields. Test cases are presented in Section 3.1 for uniform fields and in Section 3.2 for nonuniform fields. The GCA is tested in Section 3.3. Conclusions are presented in Section 4.

2. Numerical Methods

In this section, we describe the five particle movers used in this paper: the Boris method, the Vay method, the Higuera–Cary method (called HC in the remainder of the paper), the implicit midpoint method, and a method based on the GCA. We also describe our grid interpolation method. All methods have been implemented to evolve test particles in electromagnetic or MHD fields obtained from the massively parallel relativistic MHD code MPI-AMRVAC (Porth et al. 2014).

All test cases presented here involve charged particles moving in electromagnetic fields E and B. The relativistic equations of motion for such particles are (in MKS units)

$$\frac{du}{dt} = \frac{q}{m}(E + v \times B) \tag{1}$$

and

$$\frac{dx}{dt} = v, \tag{2}$$

where $u = \gamma v$ is the relativistic momentum vector divided by the particle rest mass m, $\gamma = 1/\sqrt{1 - v^2/c^2}$ is the Lorentz factor, v the velocity, q the charge, and x the particle position.

Depending on the chosen numerical approach, the equations above are integrated in some discretized form. Below, we present the integration schemes relative to the five methods used in our tests.

2.1. Explicit Leap-frog Methods

The Boris, Vay, and HC methods are designed to employ a staggered discretization in time for the position and velocity of a particle. In essence, the position at some midpoint in time is used to advance the velocity, and the velocity at some staggered point in time drives the motion in space in return. For instance, the velocity can be centered on integer time steps, and the position on half time steps. A discretized version of Equations (1)–(2) reads

$$\frac{u^{n+1} - u^n}{\Delta t} = \frac{q}{m}(E(x^{n+1/2}) + \bar{v} \times B(x^{n+1/2})), \tag{3}$$

$$\frac{x^{n+3/2} - x^{n+1/2}}{\Delta t} = v^{n+1}, \tag{4}$$

where $\bar{v}$ is some average of the velocity between two time steps that must be properly defined. It is often convenient to get rid of the staggering between position and velocity and center both quantities on integer time steps. The scheme remains essentially the same, but the operations can be reordered by splitting the position update into two half steps, one at the end of the current time iteration and the other at the beginning of the next time iteration. This operation is straightforward if one adopts the definition

$$x^n = \frac{x^{n+1/2} + x^{n-1/2}}{2}. \tag{5}$$

Such choice results in the sequence of explicit updates:

$$x^{n+1/2} = x^n + \frac{u^n}{2\gamma^n}\Delta t, \tag{6}$$

$$\frac{u^{n+1} - u^n}{\Delta t} = \frac{q}{m}(E(x^{n+1/2}) + \bar{v} \times B(x^{n+1/2})), \tag{7}$$

$$x^{n+1} = x^{n+1/2} + \frac{u^{n+1}}{2\gamma^{n+1}}\Delta t. \tag{8}$$

Note that the average velocity $\bar{v}$ on the right-hand side of Equation (7) usually involves the unknown u^{n+1}, therefore making the equation implicit. In specific cases, the expression can be formally inverted in order to obtain an explicit expression for u^{n+1}, depending on the choice of $\bar{v}$. Assuming this is possible, such a modified leapfrog scheme is composed of the following steps:

1. first half of the position update using Equation (6),
2. explicit solution for u^{n+1} by analytic inversion of Equation (7), and
3. second half of the position update using Equation (8).

This "synchronized" version of the leapfrog scheme is used for all tests shown in the next sections.

The central operation for the solution of the momentum equation is what actually distinguishes each leapfrog method. The Boris, Vay, and HC methods ultimately differ only in the definition of the average velocity, $\bar{v}$, and therefore in how the analytic inversion is carried out. A fourth explicit second-order method is presented in Qiang (2017). This method is neither time reversible nor phase-space preserving, but has the aim to perform faster while maintaining the same accuracy as the Vay integrator. Since we do not consider the computational cost of the schemes here explicitly, we have not considered this integrator in our tests.

All of these second-order explicit methods can be extended to fourth-order accuracy by employing the split-operator method (Qiang 2017). Such high-order numerical integrators can significantly save on computational cost by using a larger step size as compared with the second-order integrators. The explicit schemes retain their energy-conserving properties at higher orders, since that depends on the formulation of the average velocity, $\bar{v}$, and not on the order of the scheme (see the Appendix).

The properties of the scheme thus strongly depend on the definition of the average velocity. We are mainly interested in three properties: (1) energy conservation, (2) phase-space preservation, and (3) accurate drift motion. Energy conservation is discussed in detail in the Appendix, where it is concluded that only one specific choice of average velocity results in strict (numerical) energy conservation. Energy conservation is equivalent to the conservation of the underlying Hamiltonian. Only the implicit scheme presented in Section 2.2 conserves the Hamiltonian in the relativistic formulation. The Boris scheme conserves energy in the case of vanishing electric fields. The other schemes do not strictly conserve energy; however, in many applications the energy conservation is satisfactory. Volume preservation is attained by so-called

symplectic integrators. Symplectic integrators are designed to conserve symplectic geometries, i.e., areas in phase space: a domain of phase space is mapped by a symplectic function to a new domain of equal area (Donnelly & Rogers 2005). In addition, the energy error is bounded in such methods. Volume preservation is discussed thoroughly in Higuera & Cary (2017), concluding that the Boris scheme and the Higuera–Cary scheme are volume preserving but the Vay scheme is not. Volume preservation is defined here as the preservation of the differential volume, which is preserved by any solution of the underlying differential equation, with a finite time step (Higuera & Cary 2017). We test the preservation of the gyroradius in several different cases of magnetic and electric fields in Section 3.1. The accurate resolution of the drift motion of a particle depends on the problem settings (where Vay 2008 and Higuera & Cary 2017 mainly focus on the $E \times B$ motion) and is tested thoroughly in Sections 3.1–3.3.

2.1.1. Boris Method

The Boris method (Boris 1970) is a classic, second-order-accurate leapfrog scheme that is widely used. Even though it was first described almost 50 years ago, the method is still being actively investigated (Vay 2008; Qin et al. 2013; Ellison et al. 2015), in particular its volume-preserving and symplectic properties. For the Boris method, the definition of the average velocity is

$$\bar{v} = \frac{u^{n+1} + u^n}{2\gamma^{n+1/2}}.$$ (9)

The inversion step is then given by the following operations (see e.g., Birdsall & Langdon 1991):

1. First half electric field acceleration:

$$u^- = u^n + \frac{q\Delta t}{2m}E(x^{n+1/2}).$$ (10)

2. Rotation step:

$$u^+ = u^- + (u^- + (u^- \times t)) \times s.$$ (11)

3. Second half electric field acceleration:

$$u^{n+1} = u^+ + \frac{q\Delta t}{2m}E(x^{n+1/2}).$$ (12)

Here, the auxiliary quantities are $\gamma^- = \sqrt{1 + (u^-/c)^2}$, $\gamma^+ = \sqrt{1 + (u^+/c)^2} = \gamma^-$, $t = B(x^{n+1/2})q\Delta t/(2m\gamma^-)$, and $s = 2t/(1 + t^2)$. The pure rotation of the velocity vector to obtain u^+ results in the Lorentz factor at the midstep $\gamma^{n+1/2} = \gamma^- = \gamma^+$. In the Appendix, this property is used to show that the Boris scheme is energy conserving in case of pure magnetic fields, meaning that it preserves the property that magnetic fields do not exert work. By setting $\gamma \equiv 1$, the scheme is somewhat simplified, and one obtains a non-relativistic (Newtonian) version. When the magnetic field strength varies in space, it becomes attractive to use an adaptive time step. The time symmetry of the scheme is then lost (see e.g., Hairer 1997). Our implementation in MPI-AMRVAC supports adaptive time stepping, which has been implemented with the synchronized version of the scheme, since the same Δt can be used for both position and velocity update. However, for the tests presented here, we have employed a fixed time step.

2.1.2. Vay Method

To counteract the spurious acceleration of particles by perpendicular electric fields, Vay (2008) proposed a modification of the Boris algorithm by defining the average velocity as

$$\bar{v} = \frac{u^n/\gamma^n + u^{n+1}/\gamma^{n+1}}{2}.$$ (13)

The analytic inversion of Equation (7) is done in two steps:

1. Field contribution:

$$u^{n+1/2} = u^n + \frac{q\Delta t}{2m}\left(E(x^{n+1/2}) + \frac{u^n}{\gamma^n} \times B(x^{n+1/2})\right).$$ (14)

2. Rotation step:

$$u^{n+1} = s[u' + (u' \cdot t)t + u' \times t].$$ (15)

Here, the auxiliary quantities are given by $u' = u^{n+1/2} + E(x^{n+1/2})q\Delta t/(2m)$, $\tau = B(x^{n+1/2})q\Delta t/(2m)$, $u^* = u' \cdot \tau/c$, $\sigma = \gamma'^2 - \tau^2$, $\gamma' = \sqrt{1 + u'^2/c^2}$, $t = \tau/\gamma^{n+1}$, and $s = 1/(1 + t^2)$, with

$$\gamma^{n+1} = \sqrt{\frac{\sigma + \sqrt{\sigma^2 + 4(\tau^2 + (u^*)^2)}}{2}}.$$ (16)

The position update is done in accordance with the implemented Boris scheme by performing half the position update at the end of a step and the other half at the beginning of the next step.

2.1.3. Higuera–Cary Method

The Boris scheme is known to be volume preserving, meaning that gyration is accurately resolved. The Vay scheme is an adaptation of the Boris scheme designed to preserve the $E \times B$ velocity, which is not correctly computed with the Boris method. The Vay method is not volume preserving, which can lead to a larger error in the gyroradius. Higuera & Cary (2017) proposed a new volume-preserving method that also resolves the $E \times B$ motion accurately while keeping the computational cost similar to the Vay scheme. This method claims to conserve energy and is shown to resolve typical idealized astrophysical test cases with more accuracy than the Boris and Vay methods (Higuera & Cary 2017). The scheme relies on a new choice of the average velocity:

$$\bar{v} = \frac{u^{n+1} + u^n}{2\bar{\gamma}},$$ (17)

with

$$\bar{\gamma} = \sqrt{1 + \left(\frac{u^{n+1} + u^n}{2c}\right)^2}.$$ (18)

For this choice of $\bar{v}$, the analytic inversion of Equation (7) is performed in three steps:

1. First half electric field acceleration:

$$u^- = u^n + \frac{q\Delta t}{2m}E(x^{n+1/2}).$$ (19)

2. Rotation step:

$$u^+ = s[u^- + (u^- \cdot t)t + u^- \times t].$$ (20)

3. Second half electric field acceleration:

$$u^{n+1} = u^+ + \frac{q\Delta t}{2m}E(x^{n+1/2}) + u^- \times t.$$ (21)

Here, the auxiliary quantities are $\gamma^- = \sqrt{1 + (u^-)^2/c^2}$, $\tau = B(x^{n+1/2})q\Delta t/(2m)$, $u^* = u^- \cdot \tau/c$, $\sigma = (\gamma^-)^2 - \tau^2$, $t = \tau/\gamma^+$, and $s = 1/(1 + t^2)$, with

$$\gamma^+ = \sqrt{\frac{\sigma + \sqrt{\sigma^2 + 4(\tau^2 + (u^*)^2)}}{2}}.$$ (22)

Once again, the position update is done in accordance with the implemented Boris scheme by performing half the position update at the end of a step and the other half at the beginning of the next step.

2.2. Implicit Midpoint Method

The explicit schemes presented above allow for fast solution of the particle motion. The average velocity, $\bar{v}$, is chosen such that Equation (7) can be analytically inverted to retrieve an explicit expression for u^{n+1}. However, the split form of the position update (in our synchronized leapfrog formulation) shows that there is a discrepancy between the average velocity used to advance u, which is $\bar{v}$, and that used for x. By combining Equations (6) and (8), it follows that

$$\frac{x^{n+1} - x^n}{\Delta t} = \frac{1}{2}\left(\frac{u^{n+1}}{\gamma^{n+1}} + \frac{u^n}{\gamma^n}\right).$$ (23)

Thus, the update of the position is, in general, driven by an average velocity that may differ from the chosen form used in Equation (7). A consistent form of the system of equations addressing the latter issue reads

$$\frac{u^{n+1} - u^n}{\Delta t} = \frac{q}{m}(E(x^{n+1/2}) + \bar{v} \times B(x^{n+1/2})),$$ (24)

$$\frac{x^{n+1} - x^n}{\Delta t} = \bar{v},$$ (25)

where the update of the position is now driven by the same average velocity used in the momentum equation. The two equations are coupled through

$$x^{n+1/2} = \frac{x^{n+1} + x^n}{2},$$ (26)

and the resulting system of nonlinear equations can be reduced to a three-dimensional system using the relation

$$x^{n+1/2} = x^n + \frac{\Delta t}{2}\bar{v},$$ (27)

which differs from Equation (6). For an arbitrary choice of $\bar{v}$, it is not possible to formally invert Equation (24), and therefore one has to solve for u^{n+1} with an iterative method.

In our tests, we adopt the expression for the average velocity proposed by Lapenta & Markidis (2011),

$$\bar{v} = \frac{u^{n+1} + u^n}{\gamma^{n+1} + \gamma^n},$$ (28)

which differs from the expressions used in the Boris, Vay, and Higuera–Cary schemes. An interesting property that arises with the above definition is the conservation of energy to machine precision (Lapenta & Markidis 2011). This property suppresses spurious particle heating in, e.g., PIC simulations, avoiding the typical numerical instabilities characterizing explicit schemes (Birdsall & Langdon 1991). This is not ensured in the case of other choices of the average velocity (see the Appendix for a formal proof of the energy conservation, or a lack thereof, of all schemes). Pétri (2017) presents a fully implicit scheme similar to the one above, but with a different choice of average velocity (specifically, the one used in Vay 2008). The solution of system (24) can be carried out using several approaches (see, e.g., Noguchi et al. 2007). In this work, we choose to adopt a Newton algorithm similar to the one presented in Siddi et al. (2017) but extended here to the relativistic case. The solution algorithm is composed, at each time iteration, of the following steps:

1. The nonlinear cycle is initialized by assigning to the unknown, u_k, an initial guess u^*, where k is over the iterations. In our implementation, we find that using the value at the previous time step, u^n, proves satisfactory for all tests.
2. The kth average velocity, $\bar{v}_k$, and position, $\bar{x}_k = x_k^{n+1/2}$, are computed using u_k as the value for u^{n+1}. The field values, E and B, are interpolated at $\bar{x}_k$.
3. The kth residual is computed according to

$$F(u_k) = u_k - u^n - \frac{q\Delta t}{m}\left(E(\bar{x}_k) + \frac{u_k + u^n}{\gamma_k + \gamma^n} \times B(\bar{x}_k)\right),$$ (29)

where $\gamma_k = \sqrt{1 + u_k^2/c^2}$. The Jacobian is obtained accordingly as $J(u_k) = \partial F(u_k)/\partial u_k$ by the analytic differentiation of Equation (29) above.
4. The iteration variable is updated by solving the linear system $J(u_k)(u_{k+1} - u_k) = -F(u_k)$.
5. A termination criterion is applied, e.g., by evaluating $|u_{k+1} - u_k| < \text{tol}$, where tol is some tolerance value. We choose $\text{tol} = 10^{-14}$, slightly above double precision round off, for our tests. If the stop criterion is met, the cycle is terminated; otherwise, it is restarted by assigning $u_k = u_{k+1}$.

When the stop criterion is met, the new proper velocity is taken to be $u^{n+1} = u_{k+1}$. Finally, the new particle position is updated according to

$$x^{n+1} = x^n + \frac{u^{n+1} + u^n}{\gamma^{n+1} + \gamma^n}\Delta t.$$ (30)

In computing the Jacobian, $J(u_k)$, it is necessary to evaluate the derivatives of the field terms in Equation (29). In the most general case where such terms are obtained via interpolation from a grid, the derivatives of the fields reduce to the derivatives of the chosen interpolation function. In this work,

we choose to evaluate the fields via linear interpolation, hence dedicated routines are used to compute the corresponding interpolated derivative of the fields at the particle position. Given the residual functions (29), each term in the Jacobian matrix is usually a fairly complicated expression. For simplicity, but without loss of generality, consider the x-component of Equation (29), which reads

$$
F_x(\boldsymbol{u}) = u_x - u_x^n - \frac{q\Delta t}{m}\Bigg(E_x(\bar{\boldsymbol{x}})
$$
$$
+ \frac{u_y + u_y^n}{\gamma + \gamma^n} B_z(\bar{\boldsymbol{x}}) - \frac{u_z + u_z^n}{\gamma + \gamma^n} B_y(\bar{\boldsymbol{x}}) \Bigg). \qquad (31)
$$

Then, the first element of the Jacobian, $J_{xx}(\boldsymbol{u}) = \partial F_x(\boldsymbol{u})/\partial u_x$, is given by

$$
J_{xx}(\boldsymbol{u}) = 1 - \frac{q\Delta t}{m}\Bigg[\frac{\partial E_x(\bar{\boldsymbol{x}})}{\partial u_x} + \frac{u_y + u_y^n}{\gamma + \gamma^n}
$$
$$
\times \frac{\partial B_z(\bar{\boldsymbol{x}})}{\partial u_x} - \frac{u_z + u_z^n}{\gamma + \gamma^n}\frac{\partial B_y(\bar{\boldsymbol{x}})}{\partial u_x}
$$
$$
+ C_{2,x}(u_y + u_y^n)B_z(\bar{\boldsymbol{x}}) - C_{2,x}(u_z + u_z^n)B_y(\bar{\boldsymbol{x}})\Bigg],
$$
$$
(32)
$$

where the derivatives of the field terms are computed via the chain rule, such that, e.g., for the electric field,

$$
\frac{\partial E_x(\bar{\boldsymbol{x}})}{\partial u_x} = \frac{\partial E_x(\bar{\boldsymbol{x}})}{\partial \bar{x}}\frac{\partial \bar{x}}{\partial u_x} + \frac{\partial E_x(\bar{\boldsymbol{x}})}{\partial \bar{y}}\frac{\partial \bar{y}}{\partial u_x} + \frac{\partial E_x(\bar{\boldsymbol{x}})}{\partial \bar{z}}\frac{\partial \bar{z}}{\partial u_x}. \quad (33)
$$

This expression is convenient, since the fields are functions of the position, allowing one to use analytic derivatives (if the fields are given by an analytic expression) or take the derivative of the interpolation functions (if the fields are retrieved via interpolation). From Equations (27) and (28), the derivatives of midpoint coordinates with respect to the dimensionless four-velocity further reduce to

$$
\frac{\partial \bar{x}}{\partial u_x} = \frac{\Delta t}{2}C_{1,x}, \qquad (34)
$$

$$
\frac{\partial \bar{y}}{\partial u_x} = \frac{\partial \bar{z}}{\partial u_x} = \frac{\Delta t}{2}C_{2,x}, \qquad (35)
$$

where

$$
C_{1,i} = \frac{\partial}{\partial u_i}\left(\frac{u_i + u_i^n}{\gamma + \gamma^n}\right) = \frac{\gamma + \gamma^n - u_i(u_i + u_i^n)/(\gamma c^2)}{(\gamma + \gamma^n)^2}, \quad (36)
$$

$$
C_{2,i} = \frac{\partial}{\partial u_i}(\gamma + \gamma^n)^{-1} = -\frac{u_i/(\gamma c^2)}{(\gamma + \gamma^n)^2}, \qquad (37)
$$

which also define the coefficients in Equation (32) above. The exact same reasoning leads to the expressions of the other terms in the Jacobian matrix.

It is well known that the Newton algorithm is not guaranteed to converge. In some pathological cases, e.g., when the Jacobian vanishes at the solution, the iteration fails to converge; other non-convergence issues arise for bad choices of the initial guess or fast oscillations of the residual function around the solution. In practice, however, non-convergence is

very rarely observed for calculations in which a relatively small time step ensures that quantities do not change abruptly from one time level to the next. Nevertheless, this should not be regarded as an absolute limitation on the choice of Δt. For systems evolving according to fast dynamics, the user will be interested in capturing the details of the evolution, thus preferring a small time step; conversely, for slowly evolving systems, the algorithm is likely to converge since the change in the variables from one time level to the next will not be abrupt. A suitable choice of the initial guess represents a crucial factor in ensuring the convergence of the algorithm and should be considered carefully. When convergence is reached, in most cases the convergence rate is second order (Press et al. 1988). In our tests, we typically observe convergence to the chosen 10^{-14} absolute tolerance within four to five iterations when using the values of $\boldsymbol{u}$ at the previous time step as an initial guess for the Newton step. It is important to note that, instead of using the classical Newton algorithm with an analytical Jacobian, Jacobian-free methods (e.g., Newton–Krylov solvers; see Saad & Schultz 1986) could be adopted. The advantage of not having to compute the Jacobian, however, comes at the cost of a typically higher number of iterations needed to reach convergence.

The implicit method has the important property that it avoids the decoupling of the magnetic field advance and the electric field advance that is typical for the explicit methods. As shown by Vay (2008), this decoupling leads to the breaking of the Lorentz invariance and the introduction of spurious forces for the Boris method. The Vay method and the HC method are proven to maintain their Lorentz invariance (Vay 2008; Higuera & Cary 2017). The implicit algorithm does not decouple the electric and magnetic field advance, avoiding the problem of maintaining Lorentz invariance completely, as demonstrated in Lapenta & Markidis (2011).

2.3. The Guiding Center Approximation

In certain astrophysical circumstances, the typical length scale of the gradient in the magnetic field L is large compared to the gyroradius R_c of the particle. In this case, the gyration can be ignored for test particles. The center of the gyration (or, guiding center), rather than the actual particle position, is evolved, and the equations of motion simplify significantly, allowing for a less expensive numerical solution. The GCA is applied to Equation (1) to obtain the relativistic guiding center equations of motion describing the (change in) guiding center position $\boldsymbol{R}$, parallel relativistic momentum $m\gamma v_\parallel$, and relativistic magnetic moment $\mu_r = m\gamma^2 v_\perp^2/2B$ in three-space (Vandervoort 1960):

$$
\frac{d\boldsymbol{R}}{dt} = v_\parallel \hat{\boldsymbol{b}} - \frac{\hat{\boldsymbol{b}} \times c\boldsymbol{E}}{B} + \frac{\hat{\boldsymbol{b}}}{B\left(1 - \frac{E_\perp^2}{B^2}\right)}
$$
$$
\times \Bigg\{ \frac{cm\gamma}{q}(v_\parallel^2(\hat{\boldsymbol{b}} \cdot \nabla)\hat{\boldsymbol{b}} + v_\parallel(\boldsymbol{u}_E \cdot \nabla)\hat{\boldsymbol{b}} + v_\parallel(\hat{\boldsymbol{b}} \cdot \nabla)\boldsymbol{u}_E
$$
$$
+ (\boldsymbol{u}_E \cdot \nabla)\boldsymbol{u}_E) + \frac{\mu_r c}{\gamma q}\nabla\Bigg[B\left(1 - \frac{E_\perp^2}{B^2}\right)^{1/2}\Bigg]
$$
$$
+ \frac{v_\parallel E_\parallel}{c}\boldsymbol{u}_E \Bigg\},
$$
$$
(38)
$$

$$\frac{d(m\gamma v_{\parallel})}{dt} = m\gamma \boldsymbol{u}_E \cdot (v_{\parallel}(\hat{\boldsymbol{b}} \cdot \nabla)\hat{\boldsymbol{b}} + (\boldsymbol{u}_E \cdot \nabla)\hat{\boldsymbol{b}})$$
$$+ qE_{\parallel} - \frac{\mu_r}{\gamma}\hat{\boldsymbol{b}} \cdot \nabla \left[B \left(1 - \frac{E_{\perp}^2}{B^2} \right)^{1/2} \right], \qquad (39)$$

$$\frac{d(m\gamma^{*2}v_{\perp}^{*2}/2B^*)}{dt} = \frac{d\mu_r^*}{dt} = 0. \qquad (40)$$

Here, $\hat{\boldsymbol{b}}$ is the unit vector in the direction of the magnetic field and $v_{\parallel}$ the component of the particle velocity vector parallel to $\hat{\boldsymbol{b}}$. The magnitude of the electric field is split as $E = \sqrt{E_{\perp}^2 + E_{\parallel}^2}$, with $E_{\perp}$ the component of the electric field perpendicular to $\boldsymbol{B}$ and $E_{\parallel}$ the parallel component. The drift velocity, perpendicular to $\boldsymbol{B}$, is written as $\boldsymbol{u}_E = c\boldsymbol{E} \times \hat{\boldsymbol{b}}/B$, and $v_{\perp}^*$ is the perpendicular velocity of the particle in the frame of reference moving at $\boldsymbol{u}_E$. The magnetic field in that frame is given by $B^* = B(1 - E_{\perp}^2/B^2)^{1/2}$ up to first order. The relativistic magnetic moment μ_r^* is an adiabatic invariant and is proportional to the magnetic flux through the gyration circle, again in the frame of reference moving at $\boldsymbol{u}_E$. The oscillation of the Lorentz factor at the gyrofrequency is averaged out as well, giving $\gamma = \gamma^*(1 - E_{\perp}^2/B^2)^{-1/2}$. We assume the electromagnetic fields to be slowly varying compared to the particle dynamics, such that no temporal derivatives of electromagnetic fields appear in Equations (38)–(40).

2.3.1. Particle Drifts

For the guiding center method, we store all of the field-dependent terms in Equations (38) and (39) as grid variables and then linearly interpolate them at the location of the guiding center. This was done to improve efficiency and to avoid having to use a wider interpolation stencil to determine gradients. Having the terms in the GCA equations available provides the opportunity for information about particle drifts to be obtained. Every term in Equation (38) represents a drifting motion of the particle and every term in Equation (39) represents an acceleration mechanism. The meaning of these terms becomes clearer in the Newtonian approximation, where $v^2 \ll c^2$ and the magnitude of its $\boldsymbol{E} \times \boldsymbol{B}$ drift velocity $u_E^2 \ll c^2$ such that $\gamma \to 1$ and $1/\sqrt{(1 - E_{\perp}^2/B^2)} = 1/\sqrt{1 - u_E^2/c^2} \to 1$. Then, the relativistic magnetic moment, a constant of motion, also becomes the classical magnetic moment $\mu_r = m\gamma^2 v_{\perp}^2/2B \to \mu = mv_{\perp}^2/2B$. Applying this limit gives the Newtonian equations of motion for the guiding center:

$$\frac{d\boldsymbol{R}}{dt} = v_{\parallel}\hat{\boldsymbol{b}} + \frac{\hat{\boldsymbol{b}}}{B} \times \left\{ -c\boldsymbol{E} + \frac{cm}{q}\left(v_{\parallel}\frac{d\hat{\boldsymbol{b}}}{dt} + \frac{d\boldsymbol{u}_E}{dt} \right) \right.$$
$$\left. + \frac{\mu c}{q}\nabla B \right\}, \qquad (41)$$

$$\frac{d(mv_{\parallel})}{dt} = m\boldsymbol{u}_E \cdot \frac{d\hat{\boldsymbol{b}}}{dt} + qE_{\parallel} - \mu\hat{\boldsymbol{b}} \cdot \nabla B. \qquad (42)$$

The first term on the right-hand side of Equations (38) and (41) is the motion parallel to $\hat{\boldsymbol{b}}$ following from the solution of Equations (39) and (42), respectively. The second term in

Equations (38) and (41) is the $\boldsymbol{E} \times \boldsymbol{B}$ drift. The third term combines the curvature drift (resulting from the static part of the inertial drift) $v_{\parallel}d\hat{\boldsymbol{b}}/dt = v_{\parallel}^2(\hat{\boldsymbol{b}} \cdot \nabla)\hat{\boldsymbol{b}} + v_{\parallel}(\boldsymbol{u}_E \cdot \nabla)\hat{\boldsymbol{b}}$ and the polarization drift $d\boldsymbol{u}_E/dt = v_{\parallel}(\hat{\boldsymbol{b}} \cdot \nabla)\boldsymbol{u}_E + (\boldsymbol{u}_E \cdot \nabla)\boldsymbol{u}_E$, where non-static fields are ignored. For these drifts, the gyration period increases by a factor of γ in the relativistic Equation (38), resulting from the effective mass of the gyrating particle γm. Then, the magnitude of the magnetic field, in the frame of reference moving at $\boldsymbol{u}_E$, is $B^* = B(1 - E_{\perp}^2/B^2)^{1/2} = B\sqrt{1 - u_E^2/c^2}$ up to first order, explaining the factor $1/\sqrt{1 - u_E^2/c^2}$ appearing in all terms including the magnetic field magnitude in relativistic Equations (38) and (39). The fourth term in Equations (38) and (41) is the ∇B drift, also a factor of γ larger than it is in Equation (41). The last term on the right-hand side of Equation (38) is an additional, purely relativistic drift in the direction $\hat{\boldsymbol{b}} \times \boldsymbol{u}_E$ that is negligible in the Newtonian limit and does not appear in Equation (41) (Northrop 1963). The differences between the Newtonian and relativistic guiding center equations of motion are discussed in more detail in Ripperda et al. (2017a).

2.3.2. Runge–Kutta Method

Equations (38)–(40) are advanced with a fourth-order Runge–Kutta scheme with adaptive time stepping. Here, the particle time step δt is determined based on its parallel acceleration $a = dv_{\parallel}/dt$ and velocity $v = \sqrt{(v_{\parallel})^2 + (v_{\perp})^2}$ as the minimum of $\delta r/v$ and v/a, where δr is the grid step. This time step is restricted such that a particle cannot cross more than one grid cell in one time step. The fields $\boldsymbol{E}$ and $\boldsymbol{B}$, and for the GCA equations their spatial derivatives, are obtained at the particle position via linear interpolations in space, or they are given analytically. The particle gyroradius is also calculated at every time step and compared to the typical cell size to monitor the validity of the GCA.

2.4. Grid Interpolation

The particle movers in MPI-AMRVAC can obtain the electric and magnetic fields at a location in two ways: from a user-defined routine (e.g., an analytic function) or by (bi/tri)linear interpolation from grid variables. For the test cases presented here involving static fields with linear spatial gradients, both methods yield the same results. For more general fields, there will be an interpolation error proportional to Δx^2, i.e., the square of the grid spacing. We remark that for time-varying fields, which are not considered here, MPI-AMRVAC also performs linear interpolation in time.

For smooth fields, the use of higher-order spatial and temporal interpolation methods can greatly reduce interpolation errors. This would be particularly attractive when high-order reconstruction methods are used to compute electric and magnetic fields (see, e.g., Balsara 2009; Balsara et al. 2017). The reconstruction methods can then be re-used to interpolate the solution. However, a higher-order interpolation method requires a wider numerical stencil, which complicates the implementation near grid boundaries (Borovikov et al. 2015). Furthermore, a limiting procedure is required to avoid unrealistic interpolation values near large gradients.

MPI-AMRVAC divides the computational grid in blocks, which are distributed over the processors. Each block also contains a few layers of *ghost cells*, with data from neighboring blocks. In our current implementation, the time step is restricted so that particles cannot move more than one cell out of their current grid block. After every step of the particle movers, particles are moved to a different processor if required.

2.5. Computational Cost of Schemes

The implementation of the schemes described above has not yet been optimized for performance. Nevertheless, we here try to give a rough idea of the relative cost of the different methods. There are a number of factors to consider when judging the computational cost of a scheme, which are discussed below.

Time step restrictions—The main advantage of the GCA is that its time step is not limited by the gyration time, since gyration is ignored. All other schemes require a time step that is a fraction of the gyration time.

Cost of numerically solving the scheme's equations—The Boris method and its derivatives (Vay, Higuera–Cary) have about the same cost. For the GCA, the equations have more terms and the cost is higher, but the procedure is still explicit. For the implicit method, the cost is about four to five times that of the Boris method. For reference, we have measured the performance of the schemes for the gyration test described in Section 3.1.2. Advancing 10^3 particles over 10^4 time steps on a single 2.4 GHz processor took about 50 s with the Boris, Vay, and Higuera–Cary methods, and 2.2×10^2 s with the fully implicit method.

Interpolation costs—In order to obtain the fields at a particle position, data have to be loaded from memory and interpolated. We use linear interpolation here, for which the numerical computations are relatively cheap compared to the cost of loading data from memory. Optimizations to improve data locality, for example by sorting particles based on their position in a grid block, have yet to be made in MPI-AMRVAC.

Parallelization—The tests presented in this paper were all performed on a single processor, although our implementation also allows for parallel runs. However, we currently use the domain decomposition used for the MHD simulations to distribute the particles (i.e., load balancing does not account for test particles), which can lead to unequal load balancing and requires frequent synchronization.

3. Test Cases

In this section, we test all of the schemes presented above in idealized setups that are relevant for astrophysics. In all tests, we employ a uniform, rectilinear 3D Cartesian grid to store the field values. The grid resolution is coarse ($16 \times 16 \times 16$) in the case of uniform fields, since interpolation does not affect the results. For nonuniform fields, when interpolation is used, the resolution is specified in the corresponding sections. We adopt SI units, which are omitted in the text and figures, such that the electric field E is in Vm^{-1}, magnetic field B in T, particle charge q in C, and mass m in kg. The particle velocity v is in ms^{-1}, and the position x is in [m].

We first consider five relativistic test cases, as summarized in Table 1. Then we investigate the error in the GCA by comparing it to the Boris method in three test cases (∇B drift,

Table 1
Overview of Relativistic Test Cases

Test	Boris	Vay	HC	Implicit
Uniform E field	γ	γ	γ	γ
Uniform B field	γ		θ_c	γ
Force-free field	γ	γ, v	γ	γ, v
$E \times B$ drift				γ, R_c
Magnetic mirror	γ			γ

Note. The symbols indicate that a method has a small error (compared to the other schemes) in the Lorentz factor (γ), velocity (v), gyroradius (R_c), or gyrophase (θ_c).

magnetic null, and magnetic dipole), all in the non-relativistic regime, i.e., $\gamma \to 1$.

3.1. Uniform Static Fields

3.1.1. Uniform Electric Field

A charged particle in a uniform electric field only experiences acceleration in the direction of E. For a constant $E = (E_x, 0, 0)$, the relativistic equations of motion (1)–(2) can be solved analytically. For a particle initially at rest at the origin of the coordinate system, the result is

$$x_{an}(t) = \frac{mc^2}{qE}(\gamma_{an}(t) - 1), \qquad (43)$$

$$v_{x,an}(t) = \frac{qE}{m}\frac{t}{\gamma_{an}(t)}, \qquad (44)$$

where $\gamma_{an}(t) = \sqrt{1 + (qEt)^2/(mc)^2}$. At late times $t \gg mc/(|q|E)$, the growth of the Lorentz factor is nearly linear, whereas the velocity $v_{x,an} \approx c$.

We use the same setup described in Pétri (2017) in order to simulate the extreme acceleration of a particle with charge $q = 1$ and mass $m = 1$, up to a Lorentz factor of order $\sim 10^9$. For this purpose, we set up a uniform electric field $E_x/c = 1$, with a particle initially at rest at $x(t = 0) = (0, 0, 0)$. We let the simulation run up to $t = 10^9$ with a time step $\Delta t = 10^3$. The experiment is repeated for each integration method. The results can be directly compared to the analytic solutions above.

Figure 1 shows the relative errors measured on all quantities. All of the methods perform equally well, calculating the correct Lorentz factor. The apparent deviation of the computed γ from the exact value can be safely attributed to truncation relative to finite machine precision, since the error affecting the computed v_x is of the order of the machine precision.

The error in the position (solid lines in Figure 2) is above the machine precision for the Boris, Vay, and HC schemes, while the implicit method and the GCA perform better. This is an issue that characterizes the relativistic regime, where contrary to the Newtonian equivalent, the evolution of the velocity is nonlinear. Thus, second-order explicit schemes cannot capture the evolution of the position exactly, especially in the initial stages of acceleration (at late times, the velocity is close to the speed of light). Note that, for the same parameters, Pétri (2017) observes a much smaller error than with any explicit scheme while solving the discretized equations with an implicit scheme and the same choice of average velocity as in Vay (2008).
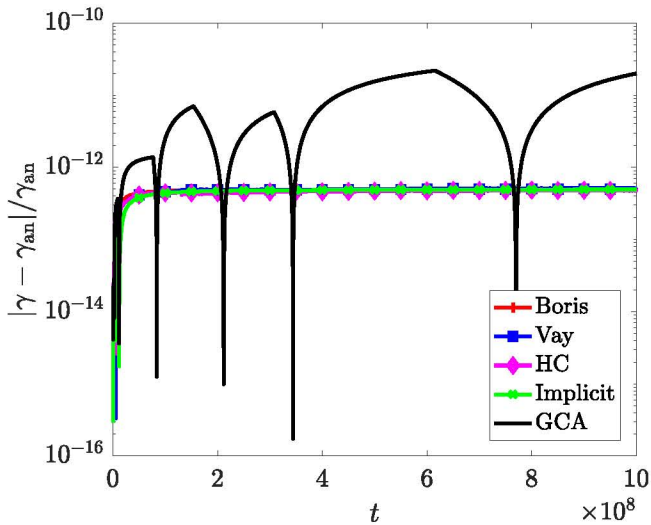
Figure 1. Relative error in γ for the uniform E field test. The errors for all methods except GCA are almost indistinguishable.
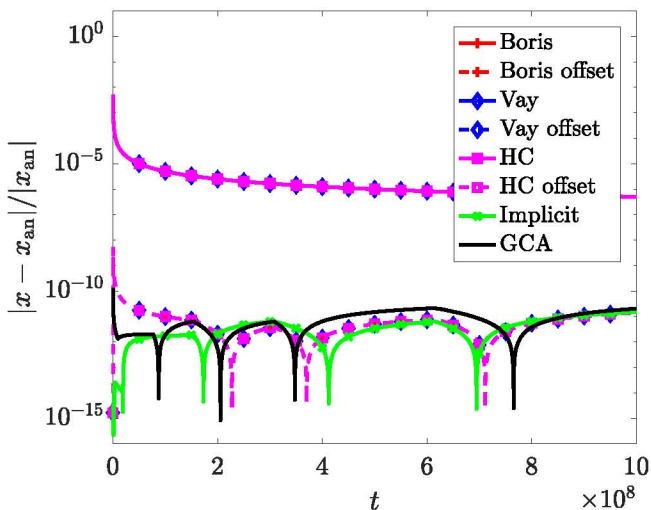
Figure 2. Relative error in the position for uniform E. The results obtained with the Boris, Vay, and HC schemes are shown with (dashed lines) and without (solid lines) an initial offset. The results for the three explicit leapfrog schemes almost perfectly overlap for both cases with and without an initial offset. The error due to the initial position is clearly pronounced here because within the initial time step, a large Lorentz factor is already reached, given the strong electric field.

The problem can be mitigated by modifying the synchronized leapfrog scheme as follows. Since the analytic solution is available, we can set the initial "real" value $x^{1/2} = x_{an}(t = 1/2)$ instead of performing a half position update at the very first iteration. This way, the value of x^1 is expected to be closer to the real value. With this modification, we run the test a second time with the explicit schemes, and we check for improvements in the computed position.

The results of both runs with and without the modified initial condition are shown in Figure 2. The error in the position, for runs with a modified initial position, is orders of magnitude smaller and comparable to the error from the GCA and implicit results. Thus, the initial offset introduced naturally by the leapfrog formulation creates a small displacement in the particle position, leading to a significantly higher error. Although using an analytic initial condition solves the problem, it is clear that this is not applicable in practice in a general case

when the real solution is not available. Note that the error in the three leapfrog explicit methods is still relatively small. In many applications, this could be acceptable compared to the cost of an implicit simulation or a higher-order RK scheme such as the one used in the GCA. For mildly relativistic regimes, this error will decrease, and in the Newtonian regime ($\gamma \to 1$), it will vanish completely. The error is pronounced clearly here because within the initial time step, a large Lorentz factor is already reached. It is also worth noting that, as reported in Pétri (2017), decreasing the time step size might not always have a positive effect, as the larger number of operations will accumulate more second-order errors.

3.1.2. Uniform Magnetic Field

A particle in a uniform magnetic field, in the absence of electric forces, gyrates in a perfect circle around the guide field line, while conserving its perpendicular velocity $v_\perp$. In the relativistic regime, the gyroradius is given by

$$R_c = \frac{\gamma m v_\perp}{|q|B},\tag{45}$$

where B is the magnitude of the guide field. The relativistic gyrofrequency $\omega_c = |q|B/(\gamma m)$ differs from its Newtonian counterpart and decreases as γ increases. Since the magnetic field does no work on the particle, γ remains constant during the gyration.

We employ the setup presented in Pétri (2017). A single particle gyrating on the gyroradius $R_c = 1$ with $\gamma = 10^6$ is initialized. The initial velocity is $v = (0, -v_\perp, 0)$, with a guide field $B = (0, 0, B_z)$. If the particle has no velocity parallel to B, the chosen γ determines $v_\perp/c = 1 - \epsilon$, with $\epsilon \simeq 5 \times 10^{-13}$. For a particle with charge $q = 1$ and mass $m = 1$, this requires a magnetic field $B_z/c \sim 10^6$. We follow the circular motion around the guiding center, located at $x_c = (0, 0, 0)$, for 100 complete turns. We choose the time step such that each complete gyration of period $T_c = 2\pi\gamma m/(|q|B)$ is resolved with 100 steps. The accuracy of the methods is determined by analyzing how well the computed γ (and therefore R_c) are conserved. We can also check for errors in the gyration phase θ_c, which is given analytically by

$$\theta_{c,an} = -\omega_c t,\tag{46}$$

where the minus sign corresponds to our choice of initial conditions. It is expected that the Boris scheme will introduce a small phase lag of order $(\Delta t)^2$ at each time step. The HC scheme will introduce a smaller phase lag of order $(\Delta t)^3$ (Higuera & Cary 2017).

Figure 3 shows the path followed by the particle during the gyration and the conservation of γ. All of the methods correctly confine the particle motion along the circle of radius 1. The GCA result is irrelevant, and it is used only as a marker for the position of the guiding center.

The conservation of γ is handled equally well by the Boris and implicit schemes. For Boris, this can be attributed to the way the Lorentz factor is calculated at each time step: if there is no electric field, the same value of γ is taken for the magnetic rotation, which in this case corresponds to the exact solution. The HC scheme produces the largest error, while the Vay scheme performs slightly better, but worse than the Boris and the implicit schemes. Contrary to the results of the previous test, these are not pure truncation errors. A deviation from the
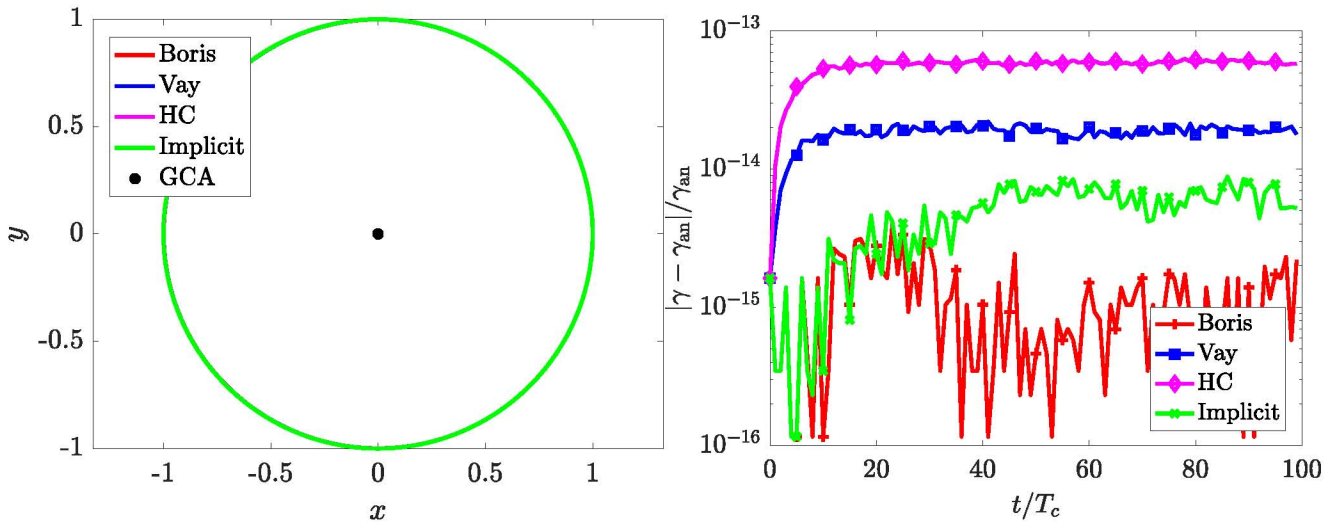
Figure 3. Results of the uniform B field test. Left: trajectory in the x–y plane. The results are visually indistinguishable for all the methods. Right: relative error in γ.

correct value of γ, in the absence of parallel motion, implies that the perpendicular velocity is varying with respect to the exact (conserved) value. The implicit solution removes the error in γ. Despite being larger, the error in the Vay and HC schemes is still extremely small and almost of the order of the machine precision, a sign that volume preservation is achieved with high accuracy. The error in γ directly translates to the error in R_c via Equation (45).

Figure 4 shows the phase lag introduced by each method. At each time step, the Boris, Vay, and implicit schemes introduce a small phase lag that accumulates over time. In our case, the gyration is shifted by ~ 0.2 radians after 100 turns. The HC scheme produces a smaller phase lag, equal to roughly half of that observed in the other methods, which is compatible with the description of the phase error in the relativistic case as described in Higuera & Cary (2017).

3.1.3. Force-free Field

In this section, we present a new test addressing the capabilities of each method in a force-free setup. In the special case $E = -v \times B$, the electric and magnetic forces cancel exactly. The resulting Lorentz force is then

$$F = q(E + v \times B) = 0, \tag{47}$$

thus there is no evolution in the particle velocity. The particle keeps on traveling at its initial speed with no net change in energy. From the numerical point of view, this test is very stringent, since a slight deviation from the exact cancellation of the field forces causes errors in the solution. In the relativistic regime, such errors propagate even more due to the coupling between velocity components through the factor γ. Note that the force-free condition cannot be obtained for an ensemble of particles with a thermal distribution, but it is still worth analyzing the situation for a single particle.

To test the strength of the schemes, we set up a particle traveling with an initial velocity v_y at $x = (0, 0, 0)$. We consider the relativistic regime $\gamma = 10^6$, setting up the electric and magnetic fields such that $E = (E_x, 0, 0)$ and $B = (0, 0, B_z)$, with $E_x = -v_y B_z$ and $B_z = 1$. The magnitude of the electric field is given by the initial particle velocity, and the force-free condition is ensured. We let the simulation run
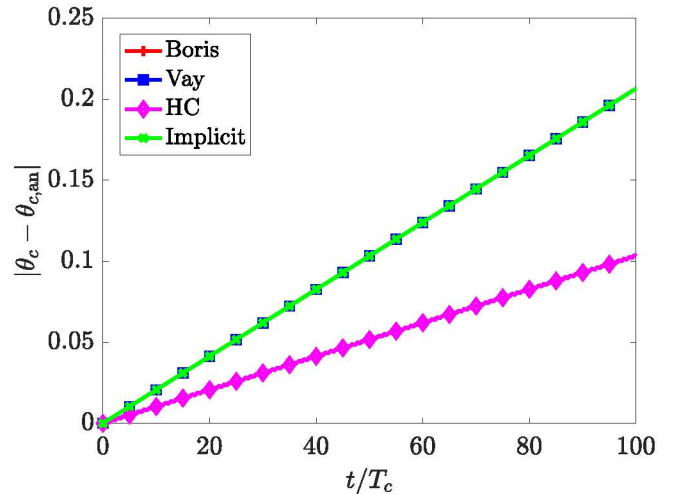

Figure 4. Phase lag absolute error for the uniform B field test. The Boris, Vay, and implicit methods show the same error, while the HC method performs better.

up to $t = 10^5$ with $\Delta t = 0.01$ and check for errors in γ and the x-position, velocity, and momentum, none of which should vary in time.

As shown in Figure 5, all methods eventually deviate from the correct position, velocity, and momentum, with the Boris scheme performing the worst, as predicted by Vay (2008). The HC scheme retains better accuracy, close to that obtained with the Vay scheme, which was designed to overcome the Boris scheme limitations in force-free conditions. The implicit scheme performs better than the others, but still produces spurious deviations from the correct trajectory. For the GCA scheme, this is a trivial test, since only the velocity parallel to B is evolved as a dynamic quantity.

For completeness, we repeat the test by varying the value of Δt. Thus, we can check how the error grows when increasing the time step for the various methods. The results are reported in Table 2, where we show the absolute error on the final particle position for each scheme. The outcome clearly shows that the error for the Boris scheme increases dramatically when increasing Δt, while for the other methods the growth is much
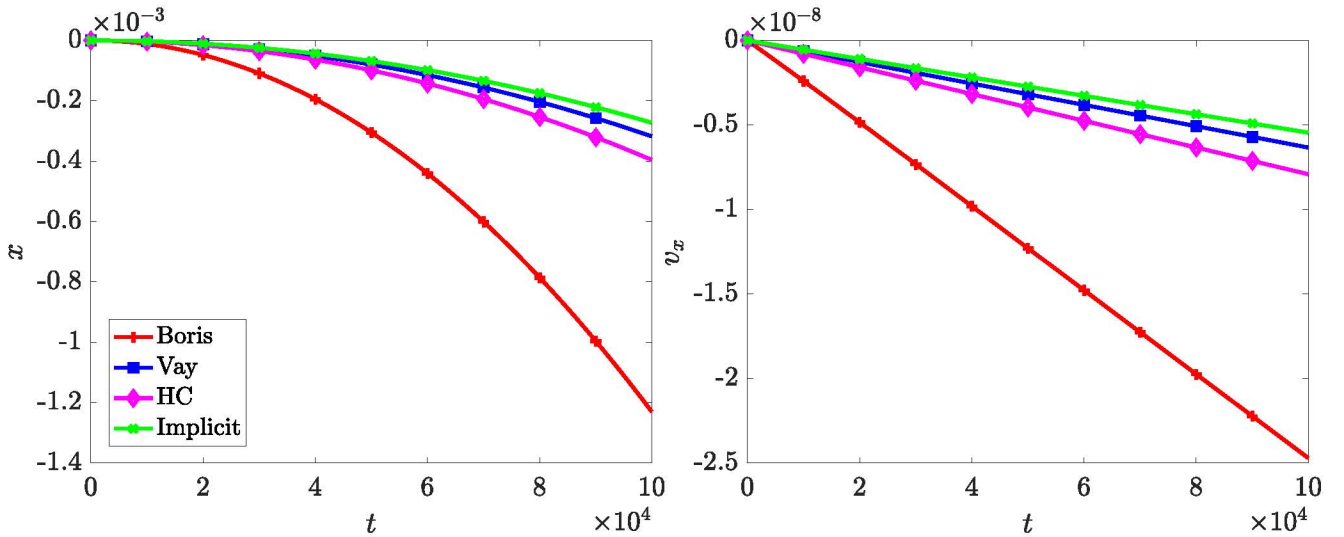
Figure 5. Results of the force-free field test. Left: deviation of the x-position from $x_{an} = 0$. Right: deviation of the x-velocity from $v_{x,an} = 0$.

Table 2
Absolute Error on the Final Particle Position Along the x-axis for the Force-free Test, for Different Δt

Δt	Boris	Vay	HC	Implicit
0.001	2.5192×10^{-2}	2.5672×10^{-2}	2.5407×10^{-2}	2.7201×10^{-2}
0.01	1.2293×10^{-1}	3.1753×10^{-2}	3.9581×10^{-2}	2.7270×10^{-2}
0.1	4.7705	3.9181×10^{-2}	5.1439×10^{-2}	2.7234×10^{-2}
1	18.7705	3.9901×10^{-2}	5.3203×10^{-2}	2.7229×10^{-2}

Note. The error affecting the Boris scheme increases approximately one order of magnitude per increasing time step, whereas for the other methods the error does not depend much on the time step.

smaller. This is consistent with the properties of the Boris scheme as explained by Vay (2008).

Interestingly, in our results, we observe no error in γ, meaning that the error in v_x is transferred to v_y with no overall change in the particle energy. This is observed for all runs at different Δt.

3.1.4. Perpendicular Electric and Magnetic Fields

In the specific case where $E = -v \times B$, all forces are canceled; however, in typical plasmas, perpendicular electric and magnetic fields ($E \cdot B = 0$) result in a drifting motion of the particle perpendicular to both fields. The average motion is in the $E \times B$ direction with drift velocity $v_E = E \times B/B^2$. This expression is only valid in the case of weak electric fields $E_\perp < cB$, with $E_\perp$ the electric field perpendicular to the magnetic field. The relativistic drift speed is measured with a Lorentz factor for the drift $\kappa = 1/\sqrt{1 - v_E^2/c^2}$. Similar to a test presented by Pétri (2017), we apply an electric field, $E = (E_0, 0, 0)$, and a magnetic field, $B = (0, 0, 1)$, with E_0 determining κ. We choose $E_0/c = 1 - \epsilon$, with $\epsilon = 5 \times 10^{-5}$ such that $\kappa = 100$. A particle with $q = 1$ and $m = 1$ is initialized at the origin $x = (0, 0, 0)$ with velocity $v = (0, 0, 0)$. We let the simulation run up to $t = 2\pi \times 10^7$ with $\Delta t = 0.5$, such that the particle undergoes 10 gyrations during its drift. The numerical experiment has also been verified for a particle in an electric field with $E_0/c = (1$–$5) \times 10^{-3}$ such that $\kappa = 10$, running up to $t = 2\pi \times 10^4$ with $\Delta t = 0.0005$.

The simulation is conducted in the observer frame, where the particle both drifts and gyrates. We analyze the results both in the observer frame and in the frame comoving with the $E \times B$ velocity. Performing a Lorentz boost on the resulting motion, from the observer frame to the $E \times B$ frame, results in a vanishing electric field and a particle gyrating along the magnetic field. In the comoving frame, this results in

$$E' = 0, \tag{48}$$

$$B' = B/\kappa. \tag{49}$$

The coordinates and velocities are boosted to the comoving frame as

$$x' = x, \tag{50}$$

$$y' = \kappa(y - v_E t), \tag{51}$$

$$z' = z, \tag{52}$$

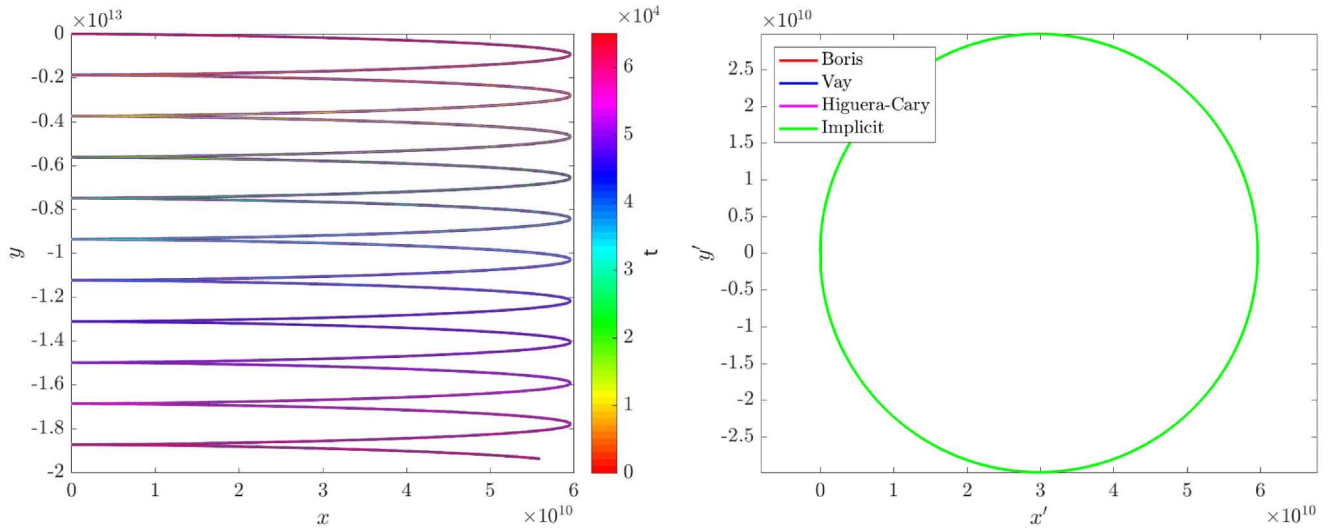$$v_x' = \frac{v_x}{\kappa} \frac{1}{1 - v_E v_y/c^2}, \tag{53}$$

$$v_y' = \left(\frac{v_y}{\kappa} - v_E + \frac{1}{c^2} \frac{\kappa v_y v_E^2}{\kappa + 1} \right) \frac{1}{1 - v_E v_y/c^2}, \tag{54}$$

$$v_z' = v_z, \tag{55}$$

resulting in a boosted Lorentz factor

$$\gamma' = \kappa \gamma \left(1 - \frac{v_E v_y}{c^2} \right). \tag{56}$$

The accuracy is measured by the error in the gyroradius in the comoving frame of reference R_c and the error in the comoving Lorentz factor γ'. Both quantities should be conserved in the comoving frame of reference. The gyroradius is calculated as

Figure 6. Trajectory of the particle colored by time in the observer frame (left-hand panel) and colored by method in the comoving $\boldsymbol{E} \times \boldsymbol{B}$ frame (right-hand panel) for $\kappa = 10$.
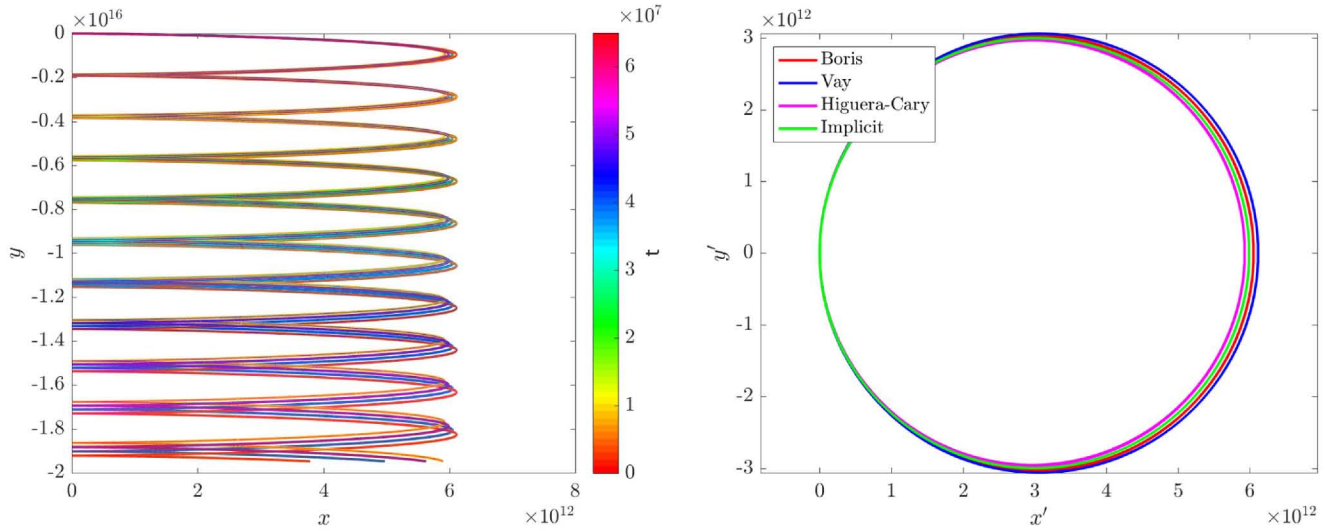
Figure 7. Trajectory of the particle colored by time in the observer frame (left-hand panel) and colored by method in the comoving $\boldsymbol{E} \times \boldsymbol{B}$ frame (right-hand panel) for $\kappa = 100$.
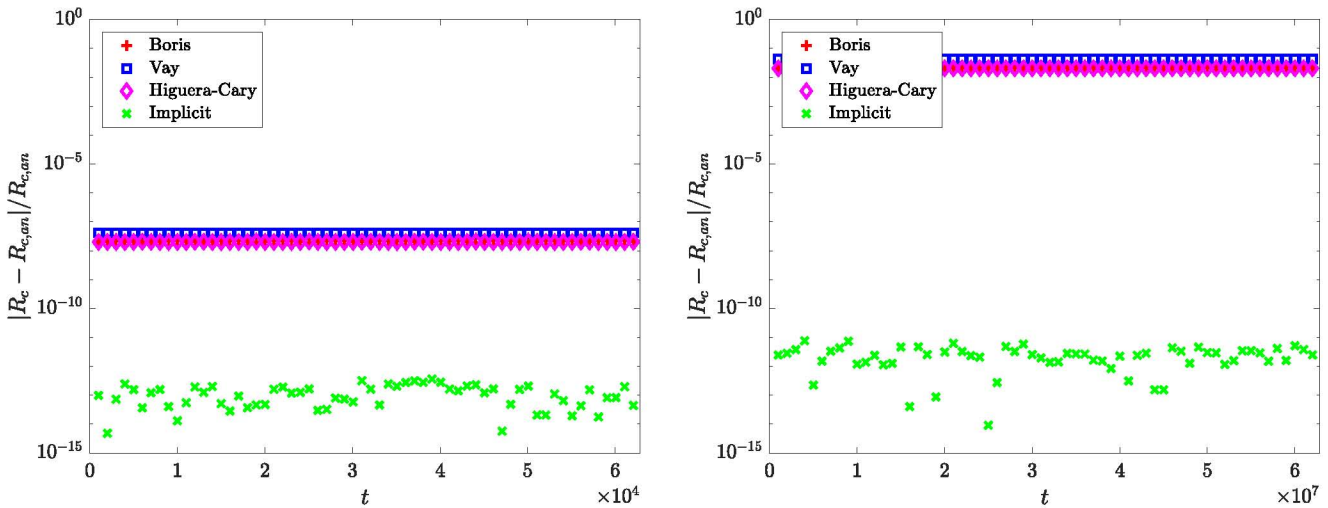
Figure 8. Relative error in the comoving gyroradius (see the right-hand panels of Figures 6 and 7) for $\kappa = 10$ (left-hand panel) and $\kappa = 100$ (right-hand panel) calculated by $R_c = m\gamma'v_\perp'/q|B'|$. The relative errors for the Boris scheme and the HC scheme overlap and are indistinguishable here, whereas they result in a different gyromotion in Figure 7.

11
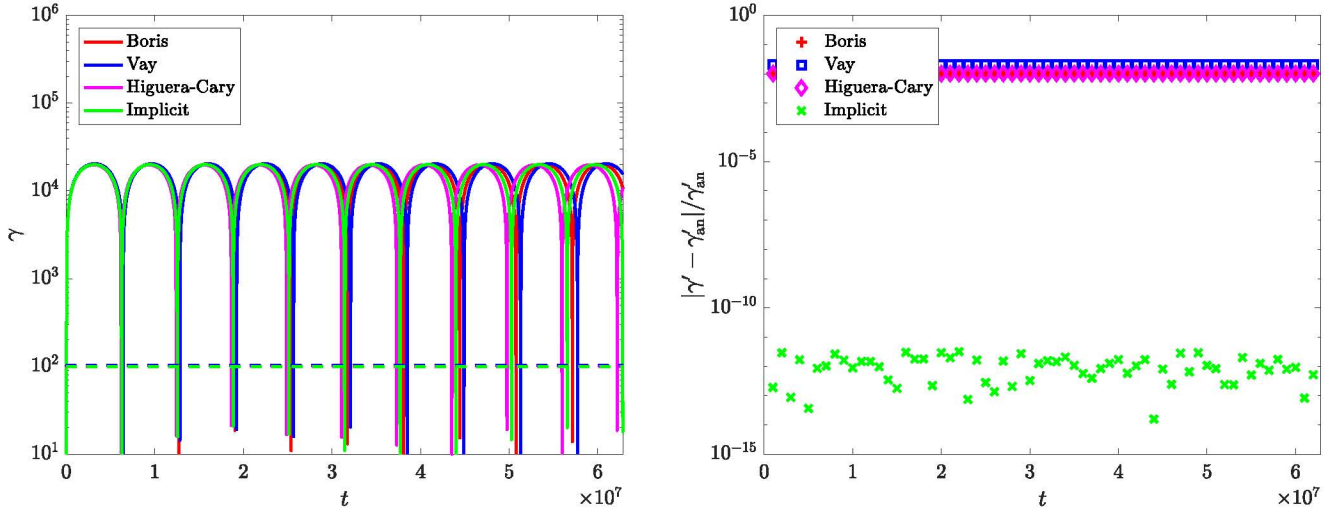
Figure 9. Lorentz factor in the observer frame (solid lines) and in the comoving frame (dashed lines) in the left-hand panel, and the relative error in the comoving Lorentz factor in the right-hand panel for $\kappa = 100$. The error for the Boris scheme and the HC scheme overlap in the right-hand panel and are indistinguishable. The error in the gyroradius $R_c = m\gamma'v_\perp/q|B'|$ in the right-hand panel of Figure 8 can be directly related to the difference in the evolution of γ in the left-hand panel of this figure and to the error in γ in the right-hand panel of this figure.

$R_c = m\gamma'v_\perp/q|B'|$. The trajectory of the particle in the observer frame is shown in the left-hand panels of Figures 6 and 7 for $\kappa = 10$ and $\kappa = 100$, respectively. The trajectory is colored by time. To distinguish between the four methods, we show the trajectory in the comoving frame in the right-hand panels. A slight deviation between the methods is visible for $\kappa = 100$, where it has to be noted that a much larger time step is used here than for the runs with $\kappa = 10$.

From the error in the gyration radius in Figure 8, for $\kappa = 10$ (left-hand side) and $\kappa = 100$ (right-hand side), it can be seen that the implicit method gives the correct gyroradius (up to machine precision), whereas all three explicit methods show a nonzero error resulting from the error in the momentum that grows for larger κ. The error in the gyroradius follows from the error in the Lorentz factor, via $R_c = m\gamma'v_\perp/q|B'|$, and not from an error in the position.

The Lorentz factor in the observer frame as determined by all four methods is shown with a solid line in the left-hand panel of Figure 9 for $\kappa = 100$. In the same plot, the dashed line represents the boosted Lorentz factor. In the right-hand panel, the relative error in the boosted Lorentz factor shows that the implicit method performs best and the Vay scheme performs worst. However, the error in the boosted Lorentz factor is not fluctuating, meaning that it remains constant but suffers from truncation errors due to the large velocities reached and the fact that we are limited by double precision accuracy. For $\kappa = 10$, the error in the Lorentz factor is six orders of magnitude smaller than that for $\kappa = 100$, and the $E \times B$ motion for the different methods is visually indistinguishable. For $\kappa = 100$, the error in the Lorentz factor results in a different evolution of γ for the different methods.

3.2. Nonuniform Static Fields

3.2.1. Magnetic Mirror

A particle can be trapped inside magnetic mirror (or bottle) configurations, meaning that the magnetic field geometry is such that the field strength increases with position. A particle traveling on a field line entering stronger magnetic fields increases its perpendicular energy as the particle gyrates faster. This increase comes at the expense of the parallel contribution to the kinetic energy since the total energy is conserved (the magnetic field does no work on the particle). The parallel velocity component decreases accordingly and will vanish at a certain point. The particle is then reflected back in the direction it came from, until it reaches the opposite side of the magnetic mirror, where it is reflected again. A typical magnetic field trapping a particle in a magnetic mirror is a quadratic function of the coordinate in the direction of the field plus a radial component,

$$\boldsymbol{B}(x, y, z) = B_0\left(1 + \frac{z^2}{L^2}\right)\hat{\boldsymbol{z}} + B_r\hat{\boldsymbol{r}}, \qquad (57)$$

with $r = \sqrt{x^2 + y^2}$. Assuming cylindrical symmetry ($\partial_\phi = 0$ and $B_\phi = 0$) for the mirror configuration, we can determine the radial component of the magnetic field via the solenoidal constraint ($\nabla \cdot \boldsymbol{B} = 0$) as (Chen 1984)

$$rB_r = -\int_0^r r'\frac{\partial B_z}{\partial z}dr' \approx -\frac{1}{2}r^2\left(\frac{\partial B_z}{\partial z}\right)_{r=0},$$

leading to

$$B_r = -rB_0\frac{z}{L^2}, \qquad (58)$$

where we have used the fact that the z-component of the magnetic field does not vary much off the axis of the magnetic mirror. We obtain the Cartesian components of the field as

$$\boldsymbol{B}(x, y, z) = -xB_0\frac{z}{L^2}\hat{\boldsymbol{x}} - yB_0\frac{z}{L^2}\hat{\boldsymbol{y}} + B_0\left(1 + \frac{z^2}{L^2}\right)\hat{\boldsymbol{z}}, \quad (59)$$

and to obtain a highly relativistic particle, we set $B_0 = 10^6$ and the gradient length $L = 10^7$. The magnetic mirror term corresponds to the last term in the right-hand side of the GCA momentum Equation (39), $-\mu_r\hat{\boldsymbol{b}} \cdot \nabla[B/\kappa]/\gamma$, or in its Newtonian limit, Equation (42), $-\mu\hat{\boldsymbol{b}} \cdot \nabla B$. The latter simplifies in the case of a mirror in the z-direction and translates to an evolution equation for $v_\parallel = v_z$, averaged over a
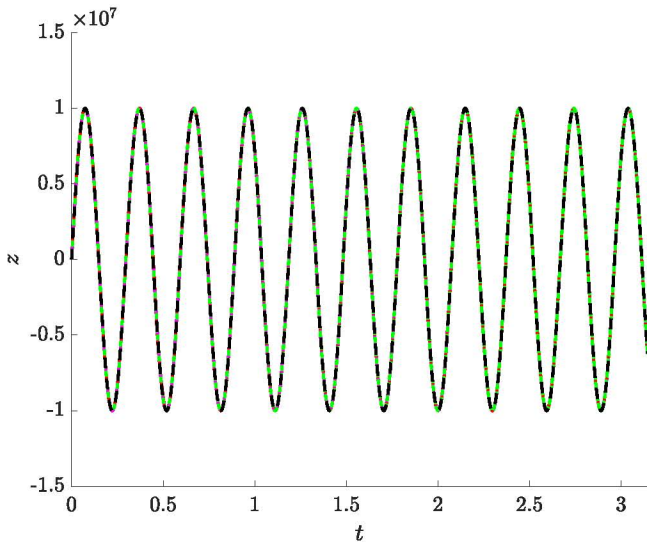
Figure 10. Particle trajectory in time on the axis of a magnetic bottle. There is no observable difference after 10 cycles through the magnetic bottle between all methods and the GCA results, here shown for the run with interpolated fields and time step $\Delta t = 10^{-8}$ for all methods, except for the Vay method, where we had to use $\Delta t = 10^{-9}$ for the particle not to escape the magnetic bottle. For all methods, the particle stays within the analytically predicted range $z_{max} = \pm 10^7$.

gyration (Chen 1984):

$$\frac{dmv_z}{dt} = -\mu \frac{\partial B_z}{\partial z}. \qquad (60)$$

We recognize the field-aligned restoring force, pointing toward the center of the magnetic mirror, opposite to the direction of increasing field strength. Particles with a purely parallel velocity (or a negligible pitch angle) have no magnetic moment μ and hence do not undergo a bouncing motion. These particles escape from the magnetic mirror, resulting in a loss cone of particles. We can obtain a condition for a particle to mirror by substituting the magnetic field given by Equation (59) in Equation (60), resulting in the mirror length (Bittencourt 2004):

$$z_{max} = \pm L \sqrt{\frac{B_{max}}{B_0} - 1} = \pm 10^7. \qquad (61)$$

However, this position depends on the assumption that the magnetic moment is conserved. The magnetic moment is an adiabatic invariant, which is only conserved to a certain extent depending on the small parameter $\epsilon = R_c/L$.

We initialize a particle with $q = 1$ and $m = 1$ at $\boldsymbol{x} = (-R_c, 0, 0)$ with velocity $\boldsymbol{v} = (0, v_\perp, v_\parallel)$ with $v_\perp = v_\parallel = 0.707c$ such that $\gamma = 100$ and the initial gyroradius is $R_c = \gamma m v_\perp/qB_0 = 0.0000707c$. The tests have been performed with time steps $\Delta t = 10^{-7}$, $\Delta t = 10^{-8}$, and $\Delta t = 10^{-9}$. The time step is decreased until the error converges such that it does not differ after taking a smaller time step. We ran with both interpolated fields and analytical fields (except for the GCA, where we always use interpolation) to rule out any effect of interpolation errors. The test with $\Delta t = 10^{-8}$ has been performed with interpolated fields with a grid resolution of $512 \times 512 \times 128$ in the domain $[-20L, 20L] \times [-20L, 20L] \times [-2 \times 10^6 L, 2 \times 10^6 L]$, and convergence has been confirmed for finer resolutions. There is no visually observable difference between the trajectory in time of the particle along the mirror axis (see Figure 10) between the explicit

methods, the implicit method, and the result from the GCA. The trajectories obtained by all methods satisfy the maximum mirror length in Equation (61). The accuracy is determined by the relative error in the Lorentz factor in the observer frame, which has to be conserved since there are no electric fields. The Lorentz factor is conserved up to machine precision by both the Boris scheme and the implicit scheme, regardless of whether the fields are given analytically or interpolated (see the left-hand panel of Figure 11 for the relative error with analytic fields and the right-hand panel for the relative error with interpolated fields). The Higuera–Cary scheme has an error that grows initially but settles to a constant value slightly larger than machine precision. The relative error in γ for the Vay scheme shows a similar trend to the Higuera–Cary scheme; however, it grows to a larger value than the error for the HC scheme, even for $\Delta t = 10^{-9}$. For a smaller time step, the error no longer decreases. The error for the Vay scheme in interpolated fields and time step $\Delta t = 10^{-8}$ is not shown because the particle's magnetic moment is not conserved due to numerical errors, and the particle escapes the magnetic bottle immediately.

We also show the error in the magnetic moment for analytic fields in the left-hand panel of Figure 12 and for interpolated fields in the right-hand panel for a fraction of the simulation up to $t = \pi/10$, corresponding to one full cycle through the magnetic bottle. It is harder to draw conclusions from this since μ is an adiabatic invariant, meaning that conservation is only approximately valid for spatially (and temporally) slowly varying fields. This is the case for $\epsilon = R_c/L \ll 1$. In our simulations, $\epsilon \approx 0.002$. For larger ϵ the error in μ grows. We do observe that the Vay scheme needs a time step that is an order of magnitude smaller than the other methods to reach the same accuracy. If we analyze the relative error in μ for the full simulation time (10 cycles through the magnetic bottle), we conclude that μ is conserved less well by the Vay scheme. This results in the particle gaining parallel velocity and losing perpendicular velocity per cycle, and eventually, the particle will leave the magnetic bottle. For interpolated fields, the error in μ is larger than that for the analytic fields, whereas for the Lorentz factor this error is of similar order. This shows that the grid resolution affects the efficiency of the mirror, and for a coarser grid, a particle will end up in the loss cone at an earlier time. For the GCA, the error in μ is equal to zero by definition.

### 3.3. Tests for the Guiding Center Approximation

With the next three test cases, we investigate the accuracy of the GCA. How well the GCA method predicts the trajectory of a gyrating particle depends on the spatial variation of the magnetic field. If during a gyration $\boldsymbol{B}$ changes significantly, the approximations employed in GCA will not be accurate. The relative change in magnetic field can be expressed as $\delta B/B$, where δB is the variation over one gyration, and B is the magnetic field at the center of gyration. An estimate for $\delta B/B$ is

$$\delta B/B \sim \frac{R_c |\nabla B|}{B}, \qquad (62)$$

where ∇B is the gradient of $|\boldsymbol{B}|$. The tests described below are performed in the non-relativistic regime ($\gamma \approx 1$) for simplicity. For relativistic particles, the validity of GCA still depends on $\delta B/B$, but then $\delta B/B$ will depend on γ since $R_c \propto \gamma$. We compare the GCA approach with the Boris method, leaving out the other particle movers described in Section 2. The reason for
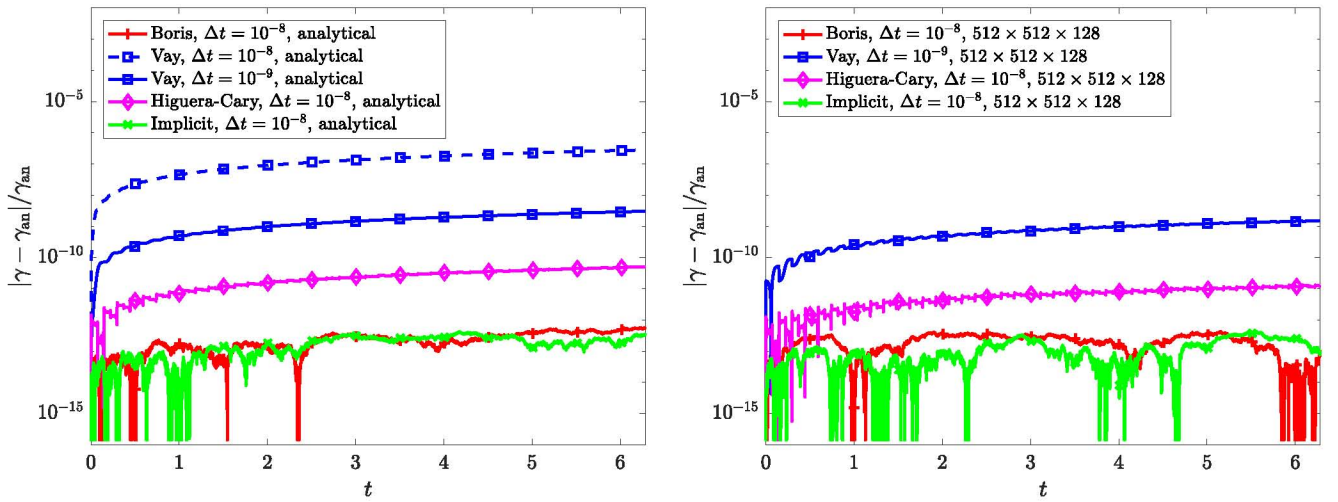
Figure 11. Relative error in the Lorentz factor with analytically given fields (left-hand panel) and interpolated fields (right-hand panel), for 10 cycles through the magnetic bottle. The error for the Vay scheme in interpolated fields and time step $\Delta t = 10^{-8}$ is not shown in the right-hand panel because the particle's magnetic moment is not conserved due to numerical errors, and the particle escapes the magnetic bottle immediately.
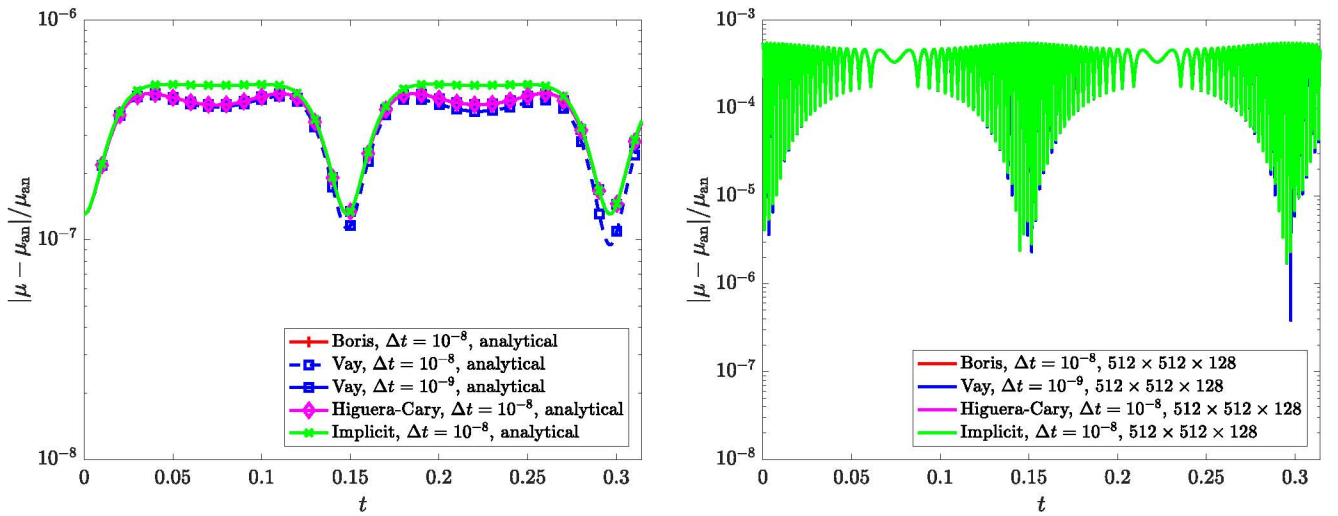
Figure 12. Relative error in the magnetic moment with analytically given fields (left-hand panel) and interpolated fields (right-hand panel) for one cycle in the magnetic bottle. The error for the Vay scheme in interpolated fields and time step $\Delta t = 10^{-8}$ is not shown in the right-hand panel because the particle's magnetic moment is not conserved due to numerical errors, and the particle escapes the magnetic bottle immediately. In the left-hand panel, for analytic fields (see the dashed blue line), the error already slightly differs after one cycle, eventually growing unboundedly until the particle escapes after a few cycles. The errors with interpolated fields (right-hand panel) are nearly identical for all methods, and much worse than those for analytical fields.

this is that for $\gamma \rightarrow 1$, the different movers (Boris, Vay, Higuera–Cary) reduce to the same scheme, and that for sufficiently small Δt the implicit scheme converges to the same results.

3.3.1. Magnetic Field Gradient

We now consider a perpendicular gradient in the magnetic field strength,

$$\boldsymbol{B}(x, y, z) = B_0 \left(1 + \frac{x}{L}\right)\hat{z}, \qquad (63)$$

and no electric field ($\boldsymbol{E} = \boldsymbol{0}$). Assuming $R_c \ll L$, the drift due to such a gradient can be approximated analytically (see, e.g., Bittencourt 2004):

$$\boldsymbol{v}_{\nabla B} = \pm \frac{v_\perp R_c}{2} \frac{\boldsymbol{B} \times \nabla B}{B^2}, \qquad (64)$$

where the $\pm$ depends on the sign of the charge of the particle, being positive for positive charges. For the field given by Equation (63) and assuming $x > -L$, this reduces to

$$\boldsymbol{v}_{\nabla B} = \pm \frac{v_\perp R_c B_0^2}{2LB^2}\left(1 + \frac{x}{L}\right)\hat{y} = \pm \frac{v_\perp R_c B_0}{2LB}\hat{y}. \qquad (65)$$

The direction of the drift is perpendicular to both the magnetic field and the direction of its gradient, so the momentum equation yields $dmv_\parallel/dt = 0$ in the absence of an electric field.

To compare the Boris scheme with the GCA, particles are created at the origin, with an initial velocity $\boldsymbol{v} = -v_0\hat{x}$. Omitting the SI units, we use $L = 1$, $q/m = 1$, and $B_0 = 1$ so that the gyration radius $R_c = v_\perp m/(qB) \approx v_0$. By varying v_0, the validity of the GCA changes, since $\delta B/B \approx v_0$. Figure 13 shows the difference in the ∇B drift velocity between the GCA and the Boris method for different values of v_0. For the Boris method, v_y was determined by fitting a line through the local minima of the y-coordinate to ensure samples were taken at the
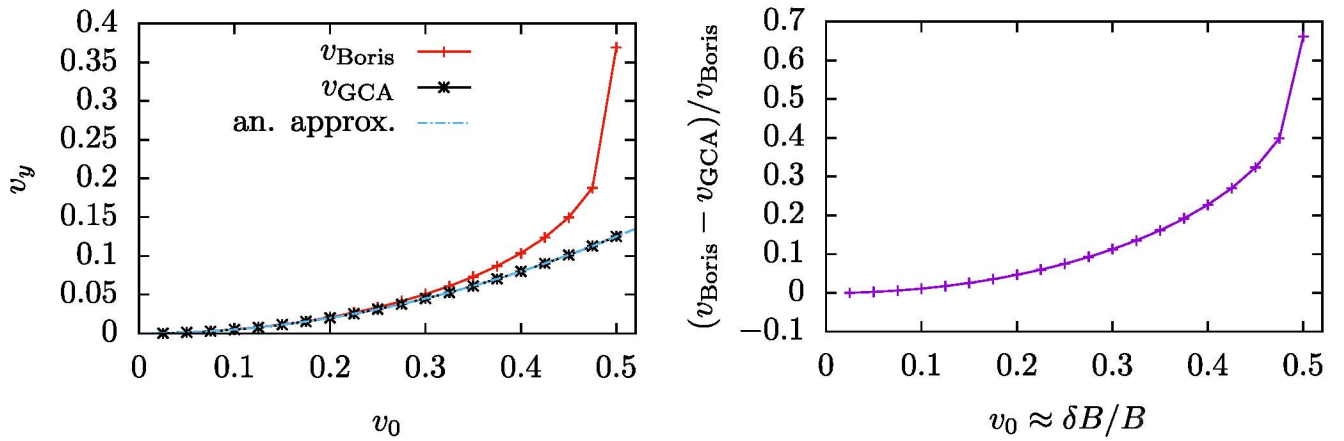
Figure 13. Left: the ∇B drift velocity v_y for a magnetic field with a linear gradient. Results are shown for the Boris method, the guiding center approximation, and for the approximation of Equation (65). Right: relative difference in the ∇B drift velocity of the GCA compared to the Boris method. For this test case, $\delta B/B \approx v_0$ (omitting SI units).

same gyration phase. Notice that for a non-relativistic particle, Equation (65) and the GCA give the same ∇B drift velocity.

For these tests, a fixed time step of $\Delta t = 5 \times 10^{-3}$ was used. The numerical grid contained $128 \times 16 \times 16$ cells, covering a computational domain of size $2\,L \times 100\,L \times 100\,L$. The reason for the extra resolution in the x-direction is to avoid interpolation errors in the GCA, which uses extra grid variables such as ∇B; see Section 2.3. The linear interpolation of such terms will not be "exact" when B_z changes sign.

Because of the relatively small time step of $\Delta t = 5 \times 10^{-3}$, the numerical errors in Figure 13 are negligible compared to the error due to the GCA. For v_0 up to 0.2, the guiding center is still in reasonably good agreement with the Boris method, showing a deviation of less than 5% in the ∇B drift velocity. However, for larger v_0 (or larger $\delta B/B$), the error increases, and the relative difference is about 65% for $v_0 = 0.5$.

3.3.2. Magnetic Null

In this example, we consider a magnetic field

$$\boldsymbol{B} = B_0\,(y/L,\ x/L,\ 0), \tag{66}$$

where we use (again omitting SI units) $L = 1$, $B_0 = 1$, and no electric field ($\boldsymbol{E} = 0$). The magnetic field, which has a null at the origin, is illustrated in Figure 14. Because of the magnetic null, the GCA is expected to fail when particles get close to the origin. To investigate this behavior, we place 500 particles on a circle in the x, y plane, centered around the z-axis (i.e., $x^2 + y^2 = 1$ and $z = 0$). All of these particles have a purely radial velocity pointing to the origin, of magnitude $v_r = -0.1$. The particles are then evolved up to $t = 30$. An example of the resulting trajectories is shown in Figure 15, both for the Boris method and the GCA.

In this example, for simplicity, particles are created at the same location, regardless of whether the GCA or Boris method is used. This leads to an error in the initial position, since the GCA particles should be initiated at the center of the gyration. However, the initial error is smallest for particles close to the diagonals, since their velocity is almost parallel to the magnetic field. We remark that in many practical applications, the

magnetic field is not known beforehand, so precisely matching the guiding centers is difficult.

When particles are located close to one of the four diagonals, their velocity is almost parallel to the magnetic field. Therefore, they will propagate toward the origin, where the GCA becomes problematic. This behavior is quantified in Figure 16, which shows the distance in particle position at $t = 30$ as computed by the GCA versus Boris method, for a varying initial angle.

For this test case, a fixed time step of $\Delta t = 5 \times 10^{-3}$ was used. The numerical grid contained $64 \times 64 \times 16$ cells, covering a domain of size $5 \times 5 \times 5$. Since the magnetic field has linear gradients, it can be interpolated "exactly" using linear interpolation. However, for some of the additional grid variables used in the GCA method, there will be an interpolation error proportional to Δx^2. This interpolation error is not the cause for the difference observed in Figure 16, which we have verified by running a test that produced nearly identical results at a twice higher resolution.

3.3.3. Dipolar Magnetic Field

The magnetic field surrounding a star or a planet, like Earth, can often be approximated by a dipole. A pure dipole has no azimuthal component and is expressed in spherical coordinates by

$$\boldsymbol{B}(r,\,\theta) = \frac{M}{r^3}[2\cos\theta\,\hat{\boldsymbol{r}} + \sin(\theta)\hat{\boldsymbol{\theta}}], \tag{67}$$

where r is the radial distance from the center of the dipole, θ is the polar angle measured from the dipole axis, and M is the dipole moment. Converting this divergence-free field to Cartesian coordinates gives

$$\boldsymbol{B}(x,\,y,\,z) = \frac{M}{(x^2 + y^2 + z^2)^{\frac{5}{2}}} \\ \times\,[3zx\hat{\boldsymbol{x}} + 3zy\hat{\boldsymbol{y}} + (2z^2 - x^2 - y^2)\hat{\boldsymbol{z}}]. \tag{68}$$

Ignoring gyration, we can estimate the gradient-curvature drift of the particle analytically. The drift velocity results from the third and fifth terms in Equation (41) and can, in the
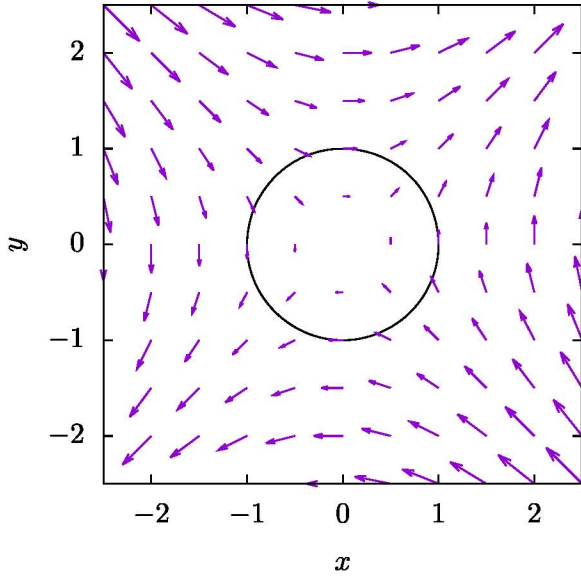
Figure 14. Magnetic field vectors in the x, y plane for the magnetic null test case in which $\boldsymbol{B} = B_0(y/L, x/L, 0)$. Initially, 500 particles are launched from the indicated unit circle, with a radially inwards velocity pointing toward the magnetic null.
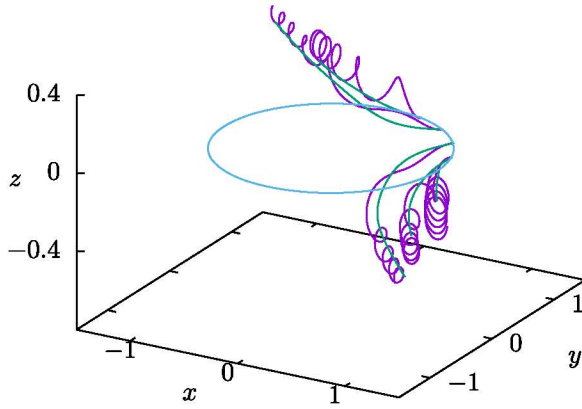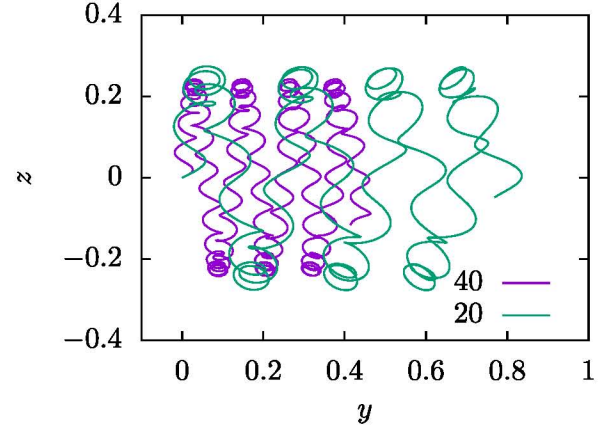

Figure 15. Examples of particle trajectories in the magnetic null case, computed with the Boris method (purple) and the GCA (green). The circle $x^2 + y^2 = 1$ on which particles are initiated is also indicated.
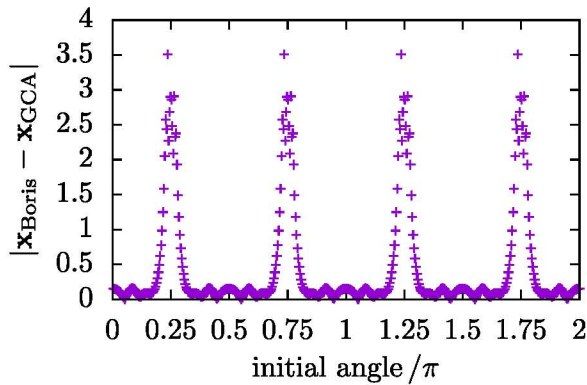
Figure 16. Distance between the predicted position at $t = 30$ with the Boris method and the GCA for the magnetic null case. The distance is shown as a function of the particles' initial ϕ angle on the circle $x^2 + y^2 = 1$. Particles close to the diagonals (at $\phi \approx \pi/4$, $3\pi/4$, $5\pi/4$, $7\pi/4$) move toward the magnetic null, where the GCA breaks down.
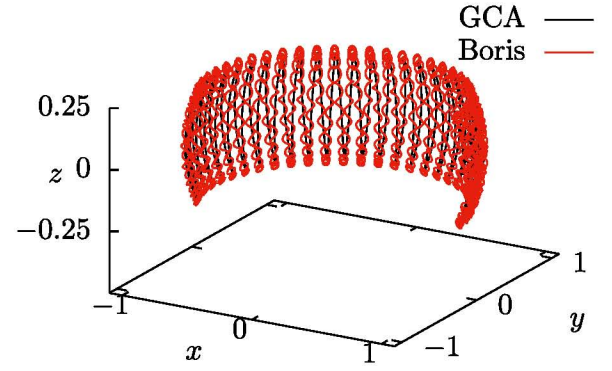
Figure 17. Example of the trajectory of a particle with $qM/m = 40$ in a dipolar magnetic field, using the Boris method and GCA. The trajectories are shown up to $t = 80$.

Figure 18. Particle trajectories in a dipolar magnetic field for $qM/m = 20$ and 40, computed with the Boris method. The trajectories are shown up to $t = 10$ and are projected along the x-axis onto the y, z plane.

absence of volume currents, be written as (Bittencourt 2004)

$$\boldsymbol{v}_{R+\nabla B} = -\frac{m}{qB^4}\left(v_\parallel^2 + \frac{1}{2}v_\perp^2\right)(\nabla B^2/2) \times \boldsymbol{B}. \tag{69}$$

For the field of Equation (67), this leads to a drift motion in the ϕ direction, for which the period is approximately (within $\sim 0.5\%$) given by Walt (1994):

$$T_{\mathrm{dipole}} \approx \frac{2\pi qM}{mv^2R_0}\left[1 - \frac{1}{3}\sin\left(\alpha_{\mathrm{eq}}\right)^{0.62}\right], \tag{70}$$

where R_0 is the equatorial distance to the guiding center, $v^2 = v_\parallel^2 + v_\perp^2$, and $\alpha_{\mathrm{eq}} = \tan^{-1}(v_\perp/v_\parallel)$ is the pitch angle at the equator. We now test how well the GCA can describe particles in a dipolar field. For these tests, the relative strength of the dipole is varied, which depends on the ratio qM/m. Omitting SI units, we take $qM/m = 10$ up to 100. Particles are placed so that their guiding center is located at $\boldsymbol{x} = (1, 0, 0)$, with an initial velocity $\boldsymbol{v} = (0, 1, 1/2)$. All particles thus have the same equatorial pitch angle α_{eq}. An example of the resulting trajectories is shown in Figure 17 for both the GCA and the Boris method. Particles exhibit both a mirror motion and a rotation in the ϕ direction. We have used a numerical grid of 256^3 cells, covering a computational domain of size $3 \times 3 \times 3$, and a fixed time step of $\Delta t = 5 \times 10^{-4}$.
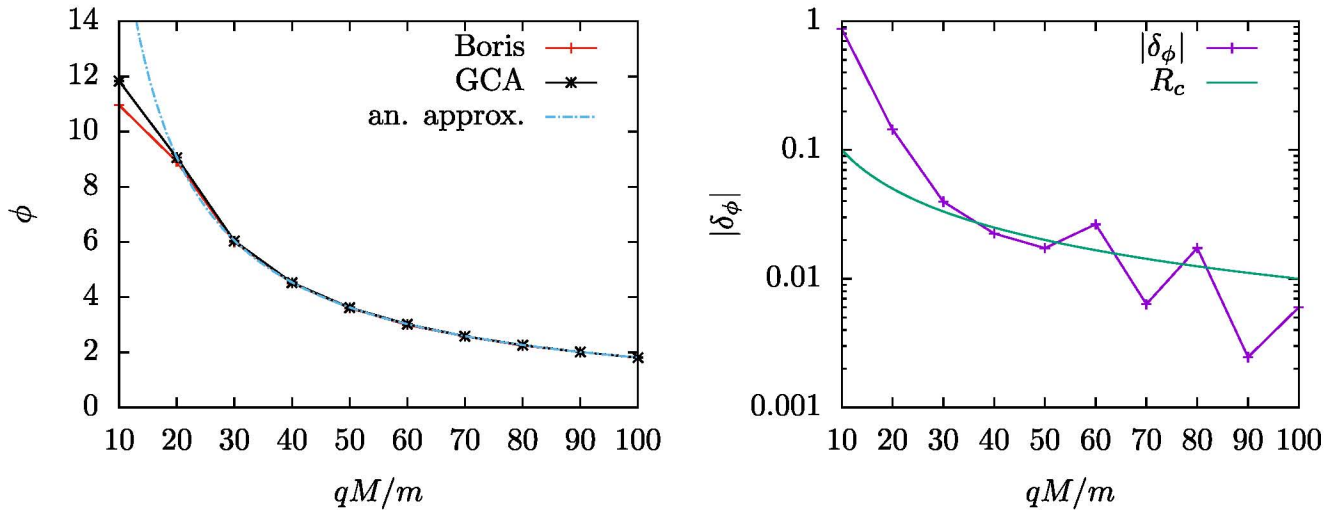
Figure 19. Left: ϕ angle after $t = 100$ for the Boris method and GCA, for particles of varying qM/m in a dipolar magnetic field. An analytic approximation $\phi = 2\pi\,(100/T_{\rm dipole})$ using Equation (70) is also shown. Right: difference in ϕ angles at $t = 100$ between the Boris method and GCA. The error in measuring ϕ for the Boris method is on the order of the gyroradius R_c, which is also indicated.

Figure 18 shows the trajectories of particles with $qM/m = 20$ and 40 up to $t = 10$, projected on to the y, z plane. A two times larger value for qM/m leads to half the rotation velocity being in the ϕ direction, as also predicted by Equation (70). Figure 19 shows how the final angle varies with qM/m, for the Boris method and GCA, and also shows the result based on Equation (70), namely $\phi = 2\pi\,(100/T_{\rm dipole})$. Because the gyration radius R_c is inversely proportional to qM/m, the GCA should improve for larger qM/m. Figure 19 also shows the difference in ϕ angles between the GCA and Boris method after $t = 100$. The agreement clearly improves up to $qM/m = 50$, after which the difference oscillates while still decreasing. The reason for this is that the angles were measured at $t = 100$ as $\phi = \tan^{-1}(y/x)$ (correcting for completed periods). For the Boris method, x, y oscillate due to particle gyration, so that the error in measuring ϕ is approximately the gyroradius R_c, which is also indicated in the figure.

In summary, we find that the GCA approximates the gradient-curvature drift in a dipolar field to high accuracy for sufficiently large qM/m. The relative error compared to the Boris method is around 1.6% for $qM/m = 20$, and rapidly decreases for larger values of qM/m.

4. Conclusions

We performed a detailed comparison between several numerical methods to solve for charged particle motion in electromagnetic fields. We compared three explicit leapfrog methods (Boris, Vay, and HC), which differ in their choice of the average velocity at half time steps, with a new implicit solution of the discretized equation of motion. The latter introduces the only average velocity expression that is fully consistent with energy conservation. These four methods to solve the Lorentz equation of motion are further compared to an adaptive Runge–Kutta integration of the relativistic version of the GCA equations. Tests deliberately explore the regime of ultrarelativistic motions, where the differences between the obtained numerical solutions become most pronounced.

Tests in uniform fields show that parallel electric field acceleration alone shows only marginal differences among these five approaches, especially in reproducing the exact proportionality between the Lorentz factor and time. For particles rapidly accelerating to high Lorentz factors, there can be offsets in the computed particle positions for the explicit methods. Ultrarelativistic gyration in a uniform magnetic field demonstrates the conservation of the Lorentz factor (and hence the gyroradius) most convincingly for both the Boris and the implicit schemes. A larger error is found in the steadily increasing phase lag of the gyration, where the HC scheme improves on the Boris, Vay, or implicit strategies. A test designed to quantify the potential weakness of all schemes for handling the equation of motion analyzes the case of a uniformly moving particle, which experiences a net zero Lorentz force. At a Lorentz factor of $\gamma = 10^6$, all except the (here trivial) GCA approach show sizable deviations in position and velocity, with the largest errors obtained when using the Boris algorithm, and the smallest ones when using the implicit scheme. All schemes keep γ constant but introduce a spurious velocity component orthogonal to the initial motion. A final test in orthogonal uniform electromagnetic fields concentrates on the $\boldsymbol{E} \times \boldsymbol{B}$ drift, and at high Lorentz factors only the new implicit method recovers the correct constant gyration radius and Lorentz factor in the comoving frame over multiple full gyration periods.

Extensions to nonuniform, static magnetic field configurations addressed issues related to magnetic mirroring and gradient-curvature drifts in idealized field prescriptions of astrophysical relevance. In a magnetic mirror (bottle) configuration, a trapped particle can maintain its Lorentz factor to machine precision when using the Boris or implicit treatments. Although the GCA approximation maintains the magnetic moment by construction, all solution methods for the Lorentz equation show sizable variations during each cycle through the bottle, and this is most notably influenced by whether analytic or interpolated electromagnetic fields are used. Field interpolations introduce larger deviations in the magnetic moment, and the Vay scheme in particular performs the worst in this aspect. Addressing interpolation effects is particularly relevant for the practical use of these schemes in PIC or MHD codes. The final three tests concentrated on Newtonian regimes, where all Lorentz solvers performed identically and where we specifically concentrated on the breakdown of the GCA

approximation. This was shown to deviate from the expected ∇B drift velocity in space-dependent magnetic fields, as soon as magnetic fields vary significantly over a gyration period. In such cases, the use of a full Lorentz solver becomes mandatory. The GCA approach is also compared with the Lorentz solver around a magnetic null point, a situation that is of prime importance for particle acceleration in reconnecting fields. This demonstrated that significant errors in the particle positions are obtained through the GCA, in particular for particles approaching the magnetic null. Finally, charged particle motions in dipolar fields can be handled well by the GCA approximation and recover the azimuthal drift along with the mirror motion as estimated by theory.

All of these methods are implemented in the open source `MPI-AMRVAC` framework (Porth et al. 2014; Xia et al. 2018) and can be used to analyze particle dynamics in evolving electromagnetic fields from MHD simulations. The extension of the methods presented here to general relativistic covariant formulations is planned for future work in the general relativistic MHD code `BHAC` (Porth et al. 2017). The implicit particle pusher that is briefly presented here will be extended to the fully implicit relativistic PIC code `xPic` (F. Bacchini et al. 2018, in preparation).

Appendix
Formal Proof of Energy Conservation

To formally prove energy conservation for our implicit particle mover, we repeat the argument of Noguchi et al. (2007) for the relativistic equation of motion. Starting from the discretized equation of motion, where n and $n + 1$ indicate consecutive time levels,

$$\frac{\boldsymbol{u}^{n+1} - \boldsymbol{u}^n}{\Delta t} = \frac{q}{m}(\boldsymbol{E}(\boldsymbol{x}^{n+1/2}) + \bar{\boldsymbol{v}} \times \boldsymbol{B}(\boldsymbol{x}^{n+1/2})), \quad (71)$$

and taking the dot product with some undefined average velocity $\bar{\boldsymbol{v}}$ on both sides,

$$\bar{\boldsymbol{v}} \cdot (\boldsymbol{u}^{n+1} - \boldsymbol{u}^n) = \frac{q\Delta t}{m}\bar{\boldsymbol{v}} \cdot \boldsymbol{E}(\boldsymbol{x}^{n+1/2}). \quad (72)$$

The magnetic field does not exert work on a particle, and the work done by an electric field is

$$\begin{aligned} W_E &= q\boldsymbol{E}(\boldsymbol{x}^{n+1/2}) \cdot \bar{\boldsymbol{v}}\Delta t \\ &= q\boldsymbol{E}(\boldsymbol{x}^{n+1/2}) \cdot (\boldsymbol{x}^{n+1} - \boldsymbol{x}^n) \\ &= mc^2(\gamma^{n+1} - \gamma^n), \end{aligned} \quad (73)$$

where we use the definition of work as the difference in kinetic energy $W_E = mc^2(\gamma^{n+1} - 1) - mc^2(\gamma^n - 1)$. This reduces to

$$\bar{\boldsymbol{v}} \cdot (\boldsymbol{u}^{n+1} - \boldsymbol{u}^n) = (\gamma^{n+1} - \gamma^n)c^2, \quad (74)$$

and gives us an energy argument to determine how $\bar{\boldsymbol{v}}$ has to be chosen to obey energy conservation for the particle mover.

A.1. Implicit Midpoint Scheme

Plugging in the velocity at half time step as used by the fully implicit scheme,

$$\bar{\boldsymbol{v}} = \frac{\boldsymbol{u}^{n+1} + \boldsymbol{u}^n}{\gamma^{n+1} + \gamma^n}, \quad (75)$$

into Equation (74) gives

$$\frac{(u^{n+1})^2 - (u^n)^2}{\gamma^{n+1} + \gamma^n} = (\gamma^{n+1} - \gamma^n)c^2, \quad (76)$$

and by using the definition of γ in terms of momentum for discretized Lorentz factors $(\gamma^{n+1})^2 = (u^{n+1})^2/c^2 + 1$ and $(\gamma^n)^2 = (u^n)^2/c^2 + 1$, we prove that equality (74) is satisfied for Equation (75).

A.2. Boris Scheme

The average velocity for the Boris scheme is given by

$$\bar{\boldsymbol{v}} = \frac{\boldsymbol{u}^{n+1} + \boldsymbol{u}^n}{2\gamma^{n+1/2}}, \quad (77)$$

with

$$\gamma^{n+1/2} = \sqrt{1 + (u^{n+1/2})^2/c^2} = \sqrt{1 + (u^-)^2/c^2}. \quad (78)$$

Plugging this $\bar{\boldsymbol{v}}$ into Equation (74), we obtain

$$\begin{aligned} \frac{\boldsymbol{u}^{n+1} + \boldsymbol{u}^n}{2\gamma^{n+1/2}} \cdot (\boldsymbol{u}^{n+1} - \boldsymbol{u}^n) &= \frac{(u^{n+1})^2 - (u^n)^2}{2\gamma^{n+1/2}} \\ &= (\gamma^{n+1} - \gamma^n)c^2, \end{aligned} \quad (79)$$

and by following the same procedure as for the implicit scheme, we find

$$\begin{aligned} \frac{(\gamma^{n+1})^2 - (\gamma^n)^2}{2\gamma^{n+1/2}} &= \frac{(\gamma^{n+1} + \gamma^n)(\gamma^{n+1} - \gamma^n)}{2\gamma^{n+1/2}} \\ &= \gamma^{n+1} - \gamma^n. \end{aligned} \quad (80)$$

This equation only holds in the specific case of $(\gamma^{n+1} + \gamma^n)/2 = \gamma^{n+1/2}$. Using the definition of $(\gamma^{n+1/2})^2 = 1 + (u^n + \epsilon)^2/c^2 = 1 + (u^{n+1} - \epsilon)^2/c^2$, with $\epsilon = (q\Delta t/2m)\boldsymbol{E}(\boldsymbol{x}^{n+1/2})$ one can show that

$$\frac{(u^{n+1})^2 - (u^n)^2}{\sqrt{1 + (u^n + \epsilon)^2/c^2} + \sqrt{1 + (u^{n+1} - \epsilon)^2/c^2}} = (\gamma^{n+1} - \gamma^n)c^2, \quad (81)$$

which is only true in the case

$$\sqrt{1 + ((u^n)^2 + 2u^n \cdot \epsilon + \epsilon^2)/c^2}$$
$$+ \sqrt{1 + ((u^{n+1})^2 - 2u^{n+1} \cdot \epsilon + \epsilon^2)/c^2}$$
$$= \sqrt{(\gamma^n)^2 + (2u^n \cdot \epsilon + \epsilon^2)/c^2}$$
$$+ \sqrt{(\gamma^{n+1})^2 + (\epsilon^2 - 2u^{n+1} \cdot \epsilon)/c^2} = \gamma^{n+1} + \gamma^n. \quad (82)$$

The equality is only satisfied in specific cases, e.g., the case of no electric field $\epsilon = 0$, which is trivial since a magnetic field does not exert work on a particle. The Boris scheme is therefore energy conserving for a vanishing electric field. However, that does not mean that a high accuracy of energy conservation cannot be obtained with a nonzero electric field.

A.3. Vay Scheme

For the Vay scheme, the choice of the average velocity is given by $\bar{v} = (v^{n+1} + v^n)/2 = (u^{n+1}/\gamma^{n+1} + u^n/\gamma^n)/2$ (Vay 2008). Plugging this $\bar{v}$ into Equation (74), we obtain

$$\left(\frac{u^{n+1}}{\gamma^{n+1}} + \frac{u^n}{\gamma^n} \right) \cdot (u^{n+1} - u^n)/2$$
$$= \frac{1}{2} \left[\frac{(u^{n+1})^2}{\gamma^{n+1}} - \frac{(u^n)^2}{\gamma^n} + \frac{u^{n+1} \cdot u^n}{\gamma^n} - \frac{u^{n+1} \cdot u^n}{\gamma^{n+1}} \right]$$
$$= \frac{1}{2} \left[\gamma^{n+1} c^2 - \gamma^n c^2 - \frac{c^2}{\gamma^{n+1}} + \frac{c^2}{\gamma^n} + u^n \cdot u^{n+1} \right.$$
$$\times \left. \left(\frac{1}{\gamma^n} - \frac{1}{\gamma^{n+1}} \right) \right] = (\gamma^{n+1} - \gamma^n)$$
$$\times \left(\frac{c^2}{2} + \frac{1}{2} \frac{u^n \cdot u^{n+1} + c^2}{\gamma^n \gamma^{n+1}} \right) \leqslant (\gamma^{n+1} - \gamma^n) c^2. \quad (83)$$

The equality is only true in the very specific case where $(u^n \cdot u^{n+1} + c^2)/(\gamma^n \gamma^{n+1}) = c^2$. The equality is satisfied if $u^n = u^{n+1}$, which is the trivial case where the particles' energy and momentum do not change. When energy conservation is not satisfied to machine precision, as is generally the case for this choice of $\bar{v}$, the particles are spuriously heated. In practice, the scheme computes particle dynamics very accurately, with bounded energy errors, but energy is not conserved in the strict sense. In an implicit scheme, based on the Vay framework (Pétri 2017), the choice of the time step will not change this; however, the number of iterations in the implicit step can result in a high accuracy for energy conservation.

A.4. Higuera–Cary Scheme

In the Higuera–Cary scheme, another average velocity is derived, which is proven to result in a volume-preserving method (Higuera & Cary 2017):

$$\bar{v} = \frac{u^{n+1} + u^n}{2\bar{\gamma}}, \quad (84)$$

$$\bar{\gamma} = \sqrt{1 + \left(\frac{u^{n+1} + u^n}{2c} \right)^2}. \quad (85)$$

Plugging this average velocity into Equation (74) results in the same final condition as for the choice of the average velocity in the Boris scheme:

$$\frac{(\gamma^{n+1} + \gamma^n)(\gamma^{n+1} - \gamma^n)}{2\gamma^{n+1/2}} = \gamma^{n+1} - \gamma^n. \quad (86)$$

This is only satisfied if

$$2 \sqrt{1 + \left(\frac{u^{n+1} + u^n}{2c} \right)^2} = \gamma^{n+1} + \gamma^n; \quad (87)$$

however,

$$2 \sqrt{1 + \left(\frac{u^{n+1} + u^n}{2c} \right)^2} =$$
$$\sqrt{[1 + (u^{n+1})^2/c^2] + [1 + (u^n)^2/c^2] + 2(1 + u^{n+1} \cdot u^n/c^2)}$$
$$= \sqrt{(\gamma^{n+1})^2 + (\gamma^n)^2 + 2(1 + (u^{n+1} \cdot u^n)/c^2)}$$
$$\leqslant \gamma^{n+1} + \gamma^n, \quad (88)$$

where the equality is only satisfied in the trivial case of a non-varying particle momentum $u^n = u^{n+1}$, resulting in the same condition as for the Vay scheme.

ORCID iDs

B. Ripperda ⓘ https://orcid.org/0000-0002-7301-3908
F. Bacchini ⓘ https://orcid.org/0000-0002-7526-8154
J. Teunissen ⓘ https://orcid.org/0000-0003-0811-5091
C. Xia ⓘ https://orcid.org/0000-0002-7153-4304
O. Porth ⓘ https://orcid.org/0000-0002-4584-2557
L. Sironi ⓘ https://orcid.org/0000-0002-5951-0756
G. Lapenta ⓘ https://orcid.org/0000-0002-3123-4024
R. Keppens ⓘ https://orcid.org/0000-0003-3544-2733

References

Bai, X., Caprioli, D., Sironi, L., & Spitkovsky, A. 2015, ApJ, 809, 55
Balsara, D. S. 2009, JCoPh, 228, 5040
Balsara, D. S., Taflove, A., Garain, S., & Montecinos, G. 2017, JCoPh, 349, 604
Birdsall, C., & Langdon, A. 1991, Plasma Physics via Computer Simulation (Bristol: IOP Publishing)
Bittencourt, J. 2004, Fundamentals of Plasma Physics (New York: Springer)
Boris, J. P. 1970, in Proc. Fourth Conf. Numerical Simulations of Plasmas (Washington, D.C.: Naval Research Laboratory), 3
Borovikov, D., Sokolov, I. V., & Tóth, G. 2015, JCoPh, 297, 599
Bowers, K. J., Albright, B. J., Yin, L., Bergen, B., & Kwan, T. J. T. 2008, PhPl, 15, 055
Buneman, O. 1993, in Computer Space Plasma Physics, ed. H. Matsumoto & Y. Omura (Tokyo: Terra Scientific), 67
Chen, F. 1984, Introduction to Plasma Physics and Controlled Fusion. Vol. 1: Plasma Physics (New York: Plenum)
Donnelly, D., & Rogers, E. 2005, AmJPh, 73, 938
Ellison, C., Burby, J., & Qin, H. 2015, JCoPh, 301, 489
Hairer, E. 1997, ApNM, 25, 219
Higuera, A., & Cary, J. 2017, PhPl, 24, 052104
Lapenta, G., & Markidis, S. 2011, PhPl, 18, 072101
Li, X., Guo, F., Li, H., & Li, G. 2015, ApJ, 811, 24
Noguchi, K., Tronci, C., Zuccaro, G., & Lapenta, G. 2007, PhPl, 14, 042308
Northrop, T. 1963, The Adiabatic Motion of Charged Particles (New York: Interscience)
Pétri, J. 2017, JPlPh, 83, 705830206
Porth, O., Olivares, H., Mizuno, Y., et al. 2017, ComAC, 4, 1
Porth, O., Vorster, M., Lyutikov, M., & Engelbrecht, N. 2016, MNRAS, 460, 4135
Porth, O., Xia, C., Hendrix, T., Moschou, S., & Keppens, R. 2014, ApJS, 214, 4

Press, W., Teukolsky, S., Vetterling, W., & Flannery, B. 1988, Numerical Recipes (Cambridge: Cambridge Univ. Press)
Qiang, J. 2017, NIMPA, 867, 15
Qin, H., Zhang, S., Xiao, J., et al. 2013, PhPl, 20, 084503
Ripperda, B., Porth, O., Xia, C., & Keppens, R. 2017a, MNRAS, 467, 3279
Ripperda, B., Porth, O., Xia, C., & Keppens, R. 2017b, MNRAS, 471, 3465
Saad, Y., & Schultz, M. 1986, SIAM J. Sci. and Stat. Comput., 7, 856
Siddi, L., Cazzola, E., & Lapenta, G. 2017, CoPhC, in press

Spitkovsky, A. 2005, in AIP Conf. Proc. 801, Astrophysical Sources of High Energy Particles and Radiation, ed. T. Bulik, B. Rudak, & G. Madejski (Melville, NY: AIP), 345
Vandervoort, P. 1960, AnPhy, 10, 401
Vay, J.-L. 2008, PhPl, 15, 056701
Walt, M. 1994, Introduction to Geomagnetically Trapped Radiation (Cambridge: Cambridge Univ. Press)
Xia, C., Teunissen, J., El Mellah, I., Chané, E., & Keppens, R. 2018, ApJS, 234, 30